

# 3D magnetic nanowire networks

# 27

Luc Piraux<sup>a</sup>, Tristan da Câmara Santa Clara Gomes<sup>a</sup>,  
Flavio Abreu Araujo<sup>a</sup>, Joaquín de la Torre Medina<sup>b</sup>

<sup>a</sup>Institute of Condensed Matter and Nanosciences, Université Catholique de Louvain, Louvain-la-Neuve, Belgium, <sup>b</sup>Morelia Unit of the Materials Research Institute of the National Autonomous University of Mexico, Morelia, Mexico

## 27.1 Introduction

The unique architectures and high degree of nanowire (NW) interconnectivity of three-dimensional (3D) NW networks make them attractive nanodevice components for a wide range of applications in energy harvesting/storage systems [1–3], electronic sensing devices and actuators [4–6], catalysts [7], electrochromic elements [8], solar cells [9], biosensors [10], and bioanalytical devices [11, 12]. However, the fabrication of 3D nanoarchitectures is extremely complicated with conventional lithography techniques and so far lacks the commercial viability. On the contrary, template-assisted synthesis is a versatile bottom-up approach for low-cost, reliable, and large-scale fabrication of NW networks with controlled size, geometry, composition, and surface morphology. Typically, these 3D networks are obtained by simple electrochemical deposition within the hierarchical nanopores of a suitable template. So far, various 3D nanoporous templates have been used for this purpose, including silica templates [13], diblock copolymers [8], 3D alumina nanoporous hosts [1, 14, 15], as well as track-etched polymeric membranes [7, 16]. The latter approach is the most promising as dense networks of crossed cylindrical nanopores can be obtained through sequential polycarbonate (PC) film irradiation with energetic heavy ions at different incidence angles, followed by selective chemical etching of the ion tracks within the polymer film [17]. The suitability of such 3D nanoporous polymer templates to form dense interconnected NW networks with tunable geometrical parameters in terms of NW size, density, and orientation opens up the possibility for a controlled synthesis of a large variety of complex 3D networks of high aspect-ratio nanostructures with different geometries and materials.

Besides, the interconnected crossed nanowires (CNWs) architecture facilitates the ability to perform magneto-transport measurements and to investigate the interplay between electronic transport and magnetic properties [18, 19], which is of paramount importance for the development of magnetic sensors and for the storage and logic operation of information carried and processed by domain walls flowing along them [20]. Also, magnetic nanotubes (NTs) are interesting cylindrical nanostructures to be arranged in a 3D morphological architecture because its magnetic and magneto-transport behavior is different to that of solid NWs. The hollow core of the NTs provides an additional geometrical degree of freedom that is responsible of modifying

magnetic states such as vortex-like structure, magnetization reversal mechanisms, and magnetic parameters like the coercive field, remanence squareness, and dipolar coupling [21–26].

On the other hand, innovative spin-based transport mechanisms are crucial steps in developing the next generation of thermoelectric materials [27]. With this perspective, coupling heat-driven transport with spintronics is at the heart of the rapidly emerging field of spin caloritronics [28, 29]. Previous studies on nanoscale metal structures, magnetic tunnel junctions, and magnetic insulators have led to the observation of various spin-enabled mechanisms that may differ significantly from conventional thermoelectrics effects such as spin Seebeck effects [30, 31], thermally driven spin injection [32], and thermal-assisted spin-transfer torque [33, 34]. However, the low conversion efficiency of the observed effects and the weak power output of the spin caloritronic devices have limited the application as heat harvesters. Another issue is the lack of established methods for reliable measurements of spin caloritronic material parameters.

It was recently demonstrated that embedding interconnected NW networks within porous polymer films provides a simple and cost-effective pathway to fabricate flexible, macroscopic-scale spin caloritronic devices. The shapeable thermoelectric films built from interconnected networks made of multilayered NWs meet key requirements for electrical, thermal, and mechanical stability and allow a precise extraction of spin-dependent Seebeck and Peltier coefficients. Moreover, the NW-based spin caloritronics devices overcome the insufficient power generation capability exhibited by the custom-patterned nanoscale magnetic structures reported previously and constitute promising candidates for heat management applications [35, 36].

In this chapter, we first briefly introduce in [Section 27.2](#) the electrochemical template-based synthesis that enable the fabrication of complex nano-architecture based on crossed magnetic nanofiber networks with controlled size, geometry, composition, and morphology. We review in [Section 27.3](#) the suitability and reliability of using interconnected NWs and NTs made of different magnetic materials of controlled composition to obtain tunable magneto-resistive behavior. Then, we show in [Section 27.4](#) how magnetic NW networks can be used as flexible, macroscopic thermoelectric devices exploiting the spin degree of freedom. Finally, the main conclusion and future perspectives are summarized in [Section 27.5](#).

## 27.2 Template-assisted electrodeposition of 3D magnetic NW and NT networks

The 3D nanoporous templates were obtained by performing a sequential multistep exposure of energetic heavy ions, at various angles with respect to the normal of PC film surface [7, 16]. Then, the latent tracks within the 20  $\mu\text{m}$  thick polymer film were chemically etched following a previously reported protocol to obtain membranes with distinct porosities and pores sizes [17]. In the present study, the as-prepared polymer membranes containing networks of interconnected cylindrical nanopores were designed with pores of well-defined diameters between 40 and 230 nm and with

different porosity characteristics ( $P = 3\%$  and  $P = 20\%$ , with  $P$  the void volume fraction of the membrane).

In the last two decades, electrodeposition has been proved to be an excellent methodology for filling host porous templates with metallic NWs with a very high degree of replication of the nanopores. Recently, the same template-based strategy was used for the synthesis of well-defined 3D architecture consisting of CNW and crossed nanotube (CNT) networks [16, 18, 19, 26]. In addition, magnetic and nonmagnetic layers were electrochemically stacked to make interconnected multilayered NWs [35, 36]. Note that after the template is filled with magnetic wires, the term packing factor is used instead of the membrane porosity, since interest is focused on the properties of NW networks. Fig. 27.1 illustrates the various 3D nanofiber architectures which have so far been investigated.

Different types of CNW networks made from pure metals (Ni, Co) and alloys (NiFe, CoNi) were grown by electrodeposition into 3D porous PC templates at room temperature (RT) via the simple potentiostatic mode [16, 18, 19]. For the purpose of preparing CNW networks, the PC templates were coated on one side with a metallic

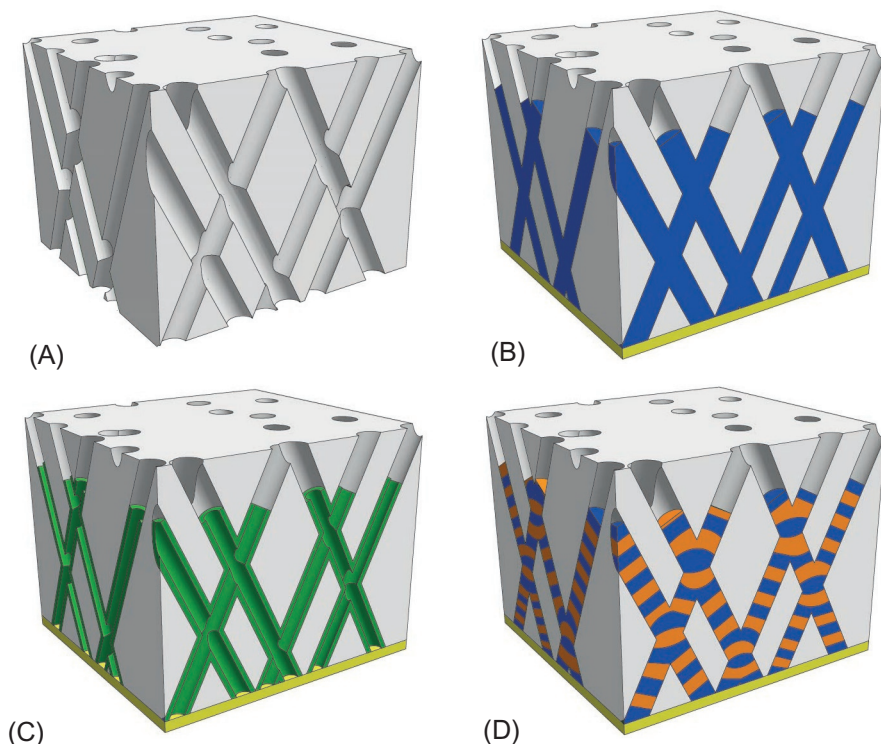


**Fig. 27.1** (A) Schematics of the 3D nanoporous polymer template, (B) crossed nanowire and (C) crossed nanotube networks, and (D) crossed nanowire network with alternating magnetic and nonmagnetic layers.

layer to serve as cathode during the electrochemical deposition. When necessary, the pH values of the as-prepared electrolytes were adjusted to the desired pH in the range 2–6.4 by addition of a diluted  $\text{H}_2\text{SO}_4$  or  $\text{HCl}$  solution or by addition of  $\text{NaOH}$ . After electrodeposition, the complete dissolution of the PC template leads to an interconnected metallic self-standing structure, as the one observed for the 40 and 230 nm diameter Ni CNW network shown in Fig. 27.2A–C. The CNW network exhibits the replicated complex NWs branching morphology of the porous template.

Over the last decade, several groups reported on the electrochemical synthesis of parallel arrays of Ni NTs within nanopores of anodic alumina oxide and polymer templates [25, 37–39]. The feasibility of using the same electrochemical method to fabricate large-scale 3D Ni CNT networks from Cu/Ni—core/shell nanocables was recently demonstrated [26]. In this method, interconnected core-shell Cu/Ni nanocables ( $\phi = 230$  nm) were grown at a constant deposition potential in the range from  $-0.8$  to  $-1.1$  V, followed by the selective electrochemical etching of the Cu-rich core at an oxidation potential of  $+0.2$  V. This process results in Ni CNT networks as

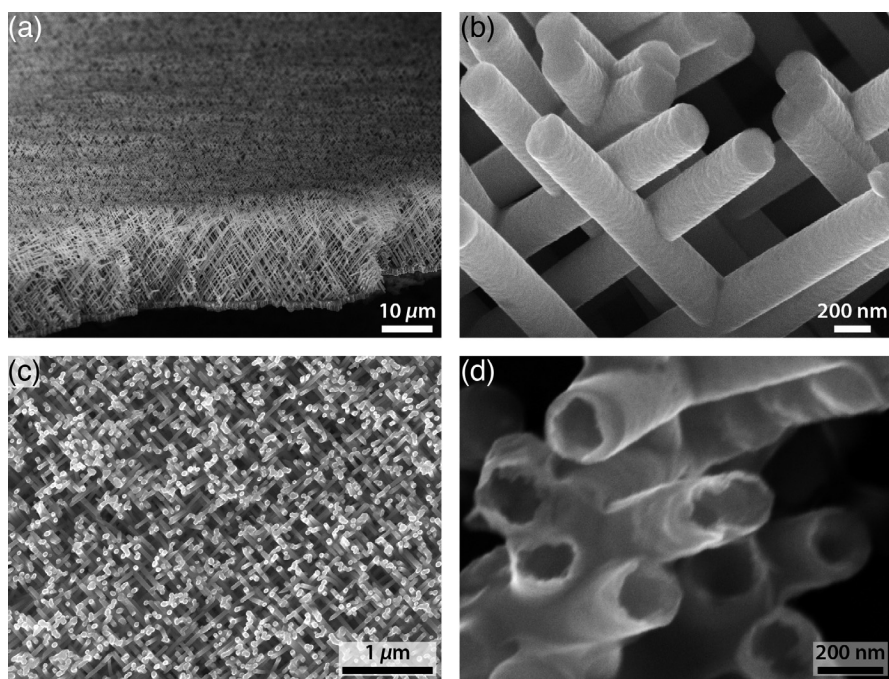


**Fig. 27.2** SEM images of self-supported interconnected nanowire and nanotube networks with different magnifications and diameters. (A) Low-magnification image showing the 50 degrees tilted view of a macroscopic nanowire network film with 230 nm diameter and (B) SEM image at higher magnification showing the nanowire branched structure. (C) Low-magnification image showing the top view of an NW network with 40 nm diameter. (D) Close magnification view of Ni crossed nanotube network with 230 nm diameter, showing the tubular structure and crossing zones of the nanotubes.

the one shown by the SEM micrograph reported in Fig. 27.2D after dissolution of the host PC membrane. Besides, since the geometrical features of the crossed core(Cu)/shell(Ni) nanocables can be carefully modified via the control over the reduction or deposition potential, Ni CNT networks with different wall thickness in the range 10–50 nm were obtained after carrying out the dealloying step of the Cu core [26].

In addition, CNWs with multilayer structure of FM/Cu, with FM = Co and equiatomic CoNi alloy, were fabricated in the host 3D porous templates [35, 36]. The multilayered NW networks have been grown at RT by electrodeposition from a single electrolyte using potentiostatic control and a pulsed electrodeposition technique [40]. To prepare the FM/Cu interconnected NW networks, the deposition potential alternatively switched between about  $-1$  V to deposit the FM layer containing approximately 5% Cu impurity, and  $-0.4$  V to deposit almost pure Cu layers. Following a procedure described elsewhere [41], the deposition rates of each metals were determined from the pore filling time. The thickness of the bilayers was set as 15 nm with approximately the same thickness for the FM and Cu layers. Interestingly, this fabrication method appears as a very convenient approach for large-scale production of current-perpendicular-to-plane (CPP) giant magneto-resistance (GMR) films based on CNW networks, as discussed in Section 27.4.

## 27.3 Interplay between the magnetic and magneto-transport properties

### 27.3.1 *Magnetic and magneto-transport properties of interconnected homogenous NW networks*

The anisotropic magneto-resistance (AMR) effect depicts the influence of the magnetization direction on the electric transport in a ferromagnetic material, and allows the local investigation of the magnetic properties. AMR is due to the anisotropy of spin-orbit scattering in transition ferromagnetic metals and leads to changes in the resistivity as the angle between the directions of the magnetization ( $M$ ) and current ( $I$ ) is modified. Despite the fact that the relative change in resistivity between the high-resistance state where the magnetization is parallel to the current ( $\rho_{\parallel}$ ) and the low-resistance state where the magnetization is perpendicular ( $\rho_{\perp}$ ) is usually small (a few percents or even less), AMR was used in previous works to study the magnetization reversal of magnetic NWs embedded within templates with parallel pores [42–44] and the magnetic properties of CNW networks [18, 19, 45]. Magneto-transport measurements were performed on homogenous CNW networks made from pure metals (Ni, Co) and alloys (NiFe, CoNi), in the temperature range from 20 K to RT, while sweeping a magnetic field between  $\pm 10$  kOe in the out-of-plane (OOP) and in-plane (IP) directions. For all samples in Section 27.3.1, the average NW diameters were 40 nm.

The experimental setup for magneto-transport shown in Fig. 27.3A is based on a four/two-probe system created at the surface of the filled template by local removing of the cathode by wet chemical etching using the iodine-based solution or by plasma

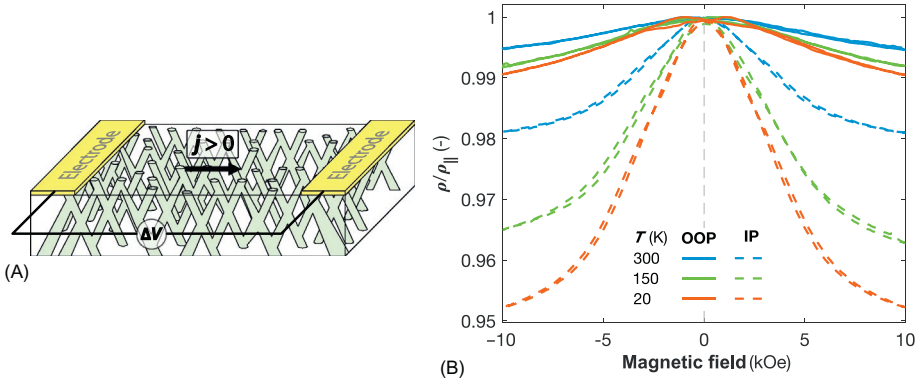


**Fig. 27.3** (A) Schematic representation of an electrode design for two-probe electrical measurement of a CNW network that partially fills a 3D porous PC membrane. (B) Anisotropic magneto-resistance curves for permalloy crossed nanowire networks measured at different temperatures by applying the external field in the OOP (*continuous lines*) and IP (*dashed lines*) directions.

etching. In this configuration, the current is directly injected to the branched CNW structure (about 1 cm long) from unetched sections of the metallic cathode, where the electrical contacts are directly made by Ag paint, and goes through the network thanks to the high degree of electrical connectivity of the CNWs. Moreover, the typical resistance values of the prepared specimens (in the range of few tens of  $\Omega$ ) is usually much larger than the ones attributed to the corresponding leads and contacts to the sample. For each sample, the input power is kept below  $0.1 \mu\text{W}$  to avoid self-heating, and the resistance was measured within its ohmic resistance range with a resolution of one part in  $10^5$ .

Fig. 27.3B shows resistance curves measured at different temperatures in the range of 20–300 K with the external field applied in the OOP and IP directions for interconnected permalloy ( $\text{Ni}_{80}\text{Fe}_{20}$ ) CNW networks, which have been found to display dominant magnetostatic (MS) contribution to the magnetic anisotropy [18]. As seen, the maximum resistance is reached near zero applied magnetic field for both directions and for all temperatures, which is consistent with remanent magnetization states where magnetization tends to be aligned with the NWs axis due to the shape anisotropy. Such a parallel configuration between current paths and local magnetization within the NW network gives rise to a high-resistance state. In the saturated state of either IP or OOP directions, the uniform distribution of NW orientations with respect to the normal plane of the membrane leads to a uniform distribution of angles between current paths and magnetization direction at saturation. In that case, resistance measurements correspond to the average magneto-resistive value resulting from the contributions of all the NWs with different orientations with respect to the applied field direction. Therefore, the resistance states at saturation ( $\bar{\rho}_{\text{IP}}$  and  $\bar{\rho}_{\text{OOP}}$ ) in both IP and OOP directions reach values which are intermediate between  $\rho_{\parallel}$  and  $\rho_{\perp}$ , with  $\bar{\rho}_{\text{IP}}$  smaller than  $\bar{\rho}_{\text{OOP}}$  given the characteristics of the membrane pore structure.

To quantitatively analyze the magneto-transport properties of the CNW networks, a model has been elaborated to account for each AMR contribution due to all the NW orientations in the 3D CNW network (see [18, 19, 45] for more info). Table 27.1 shows the AMR ratio for various CNW networks determined using this model at temperatures of 300, 150, and 20 K. The AMR ratio values for the different CNW networks are consistent with those previously reported in parallel NW arrays [41–44] and the high AMR ratio so obtained for permalloy and Ni<sub>75</sub>Co<sub>25</sub> are consistent with previous film studies [46]. The parallel configuration between  $M$  and  $I$  is identified by the maximum value,  $\rho/\rho_{\parallel} = 1$ , of the normalized resistance curve in the OOP or IP direction. Due to the reduced diameter of the NWs, this configuration is likely to be reached at  $H = 0$  in CNW networks with dominant MS contribution to the magnetic anisotropy.

A close relation between the CNWs magnetic and structural properties has also been found in Co CNWs networks ( $\phi = 40$  nm) where the effective magnetic anisotropy and absorption frequency of Co CNW networks can be strongly modified using well-known mechanisms to modify their microstructure, such as the electrolyte pH [18, 47]. Indeed, the combination of MS effects and magnetocrystalline (MC) anisotropy, together with the peculiar geometrical arrangements and suitable choice of material composition, enables for the design of 3D CNW networks with tunable static and dynamic magnetic properties. Fig. 27.4A shows the OOP hysteresis loops measured at RT on permalloy CNW network and Co CNW networks deposited at pH 2.0, 5.0, and 6.4, plotted as a function of the  $H/H_c$  ratio, with  $H_c$  their corresponding coercive field. As seen, Co CNWs display different magnetic and structural properties by an appropriate choice of pH. Considering the Co CNWs prepared at pH 2.0, the effective anisotropy is found to be entirely MS as in the NiFe CNWs. Indeed, for purely MS systems, the coercive field is proportional to the saturation magnetization  $M_s$ . Therefore, the ratio  $H/H_c$  is independent on the magnetic material of the NWs and reflects the same structural factor for all CNW networks with dominant MS contribution to the magnetic anisotropy. Indeed, the very good agreement between the hysteresis loops for permalloy and Co pH 2.0 shows that their magnetic behaviors are the same and thus of MS origin. It has been found that Co CNWs grown in an electrolyte at a pH value of 2.0 show no favorable structural texture, as revealed by X-ray diffraction

**Table 27.1** Values of the AMR ratio for Ni, Ni<sub>80</sub>Fe<sub>20</sub>, and Ni<sub>75</sub>Co<sub>25</sub> CNW networks at different temperatures.

Sample	$T$ (K)	AMR (%)
Ni	300	1.56
	150	1.16
	20	0.17
Ni <sub>80</sub> Fe <sub>20</sub>	300	2.87
	150	4.60
	20	5.48
Ni <sub>75</sub> Co <sub>25</sub>	300	4.00
	150	6.29
	20	9.07

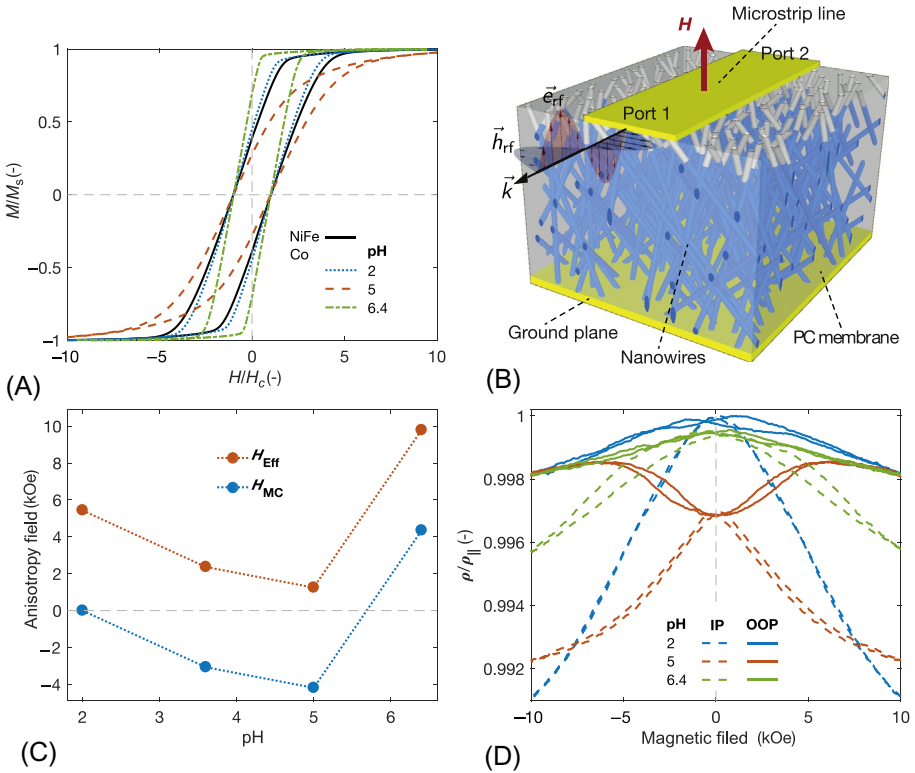


**Fig. 27.4** (A) Comparison between the OOP hysteresis loops for the NiFe and electrodeposited Co CNW networks ( $\phi = 40$  nm) using different electrolytic bath acidities of pH 2.0, 5.0, and 6.4, plotted versus the field ratio  $H/H_c$ , where  $H_c$  is the corresponding coercive field. Magnetization curves were obtained using an alternating gradient field magnetometer. (B) Schematic of a stripline transmission line for FMR measurement fabricated using a 3D polymer membrane with partially filled pores. (C) Variation of the anisotropy fields  $H_{\text{Eff}}$  and  $H_{\text{MC}}$  versus pH of electrolyte solution for Co CNW networks. *Dotted lines* are guides for the eye. (D) Room temperature AMR curves for the Co CNW networks of (A).

(XRD) analysis [18]. A very significant reduction of the magnetic anisotropy is found for the Co CNWs prepared at pH value 5.0, where a preferential texture with the HCP  $c$ -axis perpendicular to the NWs axis has been found by XRD analysis. This results in a competition between MS and transverse MC anisotropies, leading to lower remanence and coercivity in the OOP direction. In contrast, a very large increase in the effective anisotropy is observed in the Co CNWs prepared at pH value 6.4, which favors a HCP  $c$ -axis parallel to the NWs, as confirmed by XRD analysis, thus resulting in an additive MC contribution to the total anisotropy field. In this case, the squareness in the OOP direction is also strongly enhanced, which is consistent with the properties expected for low diameter NWs with strong uniaxial magnetic anisotropy. For this particular sample (pH 6.4), the field required to reach saturation magnetization in

the IP direction is larger than 10 kOe. These relations between pH induced structural changes in Co CNWs and their total magnetic anisotropy are in very good agreement with previous results obtained in arrays of parallel Co NWs [47].

Ferromagnetic resonance (FMR) measurements provide further information about the magnetic properties of the distinct CNW networks. As shown in Fig. 27.4B, a 500  $\mu\text{m}$  wide and 500 nm thick microstrip line wave-guide was evaporated on the free surface of the PC membrane after electrodeposition. FMR measurements were performed at RT at a constant frequency in the range of 100 MHz to 50 GHz, by sweeping the magnetic field applied in the OOP direction from 10 kOe down to zero field. Fig. 27.4C shows the variation of the effective anisotropy fields  $H_{\text{Eff}}$  and the MC contributions in the anisotropy field  $H_{\text{MC}}$  in function of the solution pH for Co CNW networks obtained from the FMR measurement (see [18] for details). As seen, for Co (pH 2.0) CNW networks, only MS contributions are present in the anisotropy field ( $H_{\text{Eff}} = H_{\text{MS}} = 5.44$  kOe, with  $H_{\text{MS}}$  the MS contributions in the anisotropy field). In contrast, for the case of Co CNW networks with MC contributions,  $H_{\text{Eff}} = H_{\text{MS}} \pm H_{\text{MC}}$ . For the case of the pH 3.4 and 5.0 samples, the  $H_{\text{MC}}$  is negative and reaches a minimum of  $-4.20$  kOe, while  $H_{\text{MC}}$  is positive for the pH 6.4 sample and reaches 4.35 kOe. Particularly,  $H_{\text{Eff}}$  has the lowest value for the Co (pH 5.0) sample as it is nearly isotropic.

Fig. 27.4D shows the resistance curves measured at RT with the external field in the OOP (continuous lines) and IP (dashed lines) directions for interconnected Co CNW networks deposited at pH 2.0, 5.0, and 6.4. For the FCC-like Co (pH 2) CNW network that has only MS contributions,  $\rho_{\parallel} = \rho(H = 0)$  by analogy with the permalloy CNW network shown in Fig. 27.3A. For a pH value of 5.0, the reduced value of  $\rho/\rho_{\parallel}$  at  $H = 0$  is a clear signature of a significant magnetization components perpendicular to the NWs in the remanent state due to the transverse MC anisotropy and is in agreement with the hysteresis loops and the FMR results in Fig. 27.4A and C. Also in accordance with the hysteresis loops in Fig. 27.4A, the Co CNW network obtained at pH 6.4 did not reach magnetic saturation at the maximum applied field in the IP direction. In contrast, similar resistance saturation is reached at saturation in the IP and OOP direction for interconnected Co CNW networks deposited at pH in the range 2.0–5.0, as the AMR effect is independent of the bath acidity [18]. An AMR ratio of  $\sim 1\%$  has been found for the Co CNW networks using the reported model inherent to the morphology of the studied system [18].

Considering NiCo alloy CNW networks, the magnetic anisotropy has been found dependent on the alloying composition. Fig. 27.5A shows the RT hysteresis loops measured with the field applied in the OOP directions for  $\text{Ni}_x\text{Co}_{1-x}$  ( $0 \leq x \leq 1$ ) CNW networks, plotted as a function of the  $H/H_c$  ratio. As seen, Ni and Ni-rich (with  $x > 45\%$ ) NiCo samples display fair square hysteresis loops in contrast to the case of the Co (pH 5) and Co-rich NiCo. Decreasing the Ni content below 45% leads to the appearance of a transverse HCP MC anisotropy contribution, which competes with the MS anisotropy contribution, since the  $c$ -axis is perpendicular to the NWs axis, as revealed by XRD analysis [18, 19]. Therefore, the magnetic anisotropy in OOP of Ni-rich networks is higher than that of Co-rich ones, as expected. Fig. 27.5B shows the MC field  $H_{\text{MC}}$  as a function of the Ni content ( $x$ ), obtained by FMR measurements on several  $\text{Ni}_x\text{Co}_{1-x}$  alloy CNW networks. As expected,  $H_{\text{MC}}$  is negative and increases

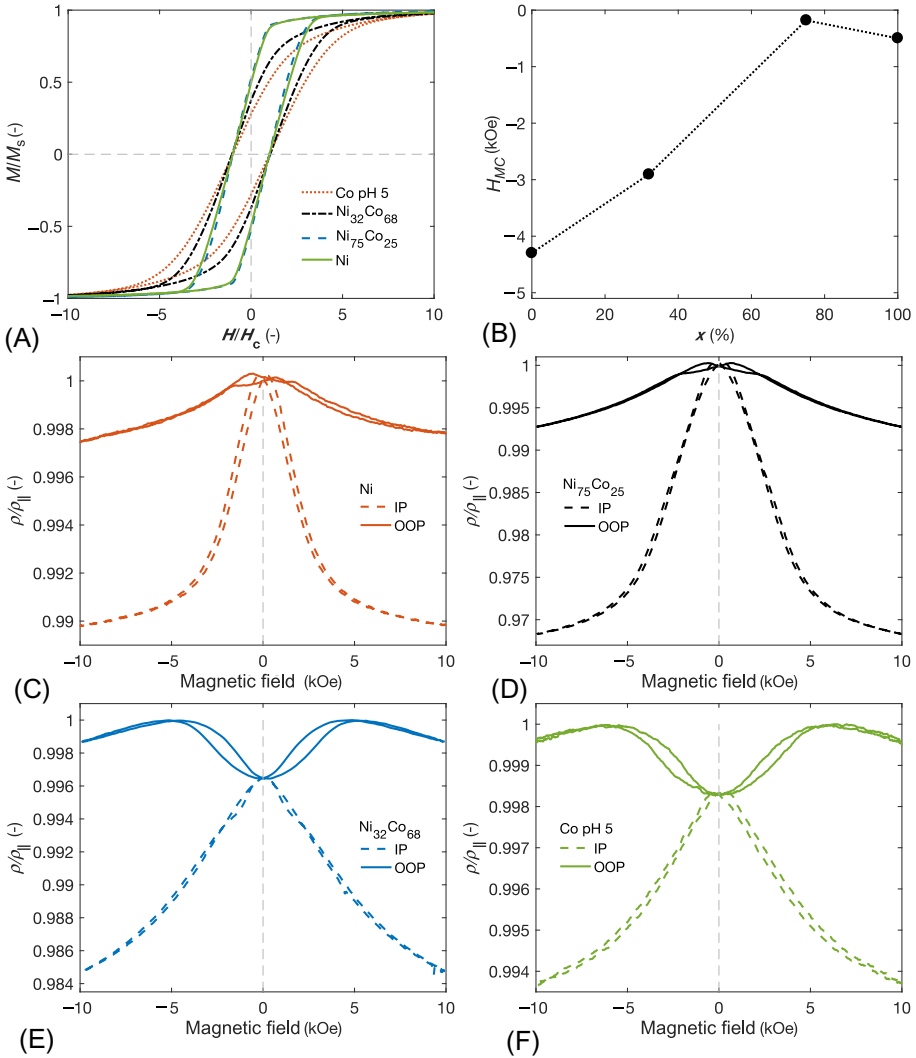


**Fig. 27.5** (A) Comparison between the OOP hysteresis loops for various Ni<sub>x</sub>Co<sub>1-x</sub> CNW networks, with  $0 \leq x \leq 1$ , plotted versus the field ratio  $H/H_c$ , where  $H_c$  is the corresponding coercive field. (B) Variation of the magnetocrystalline contributions in the anisotropy field  $H_{MC}$  as a function of the Ni content ( $x$ ) for the NiCo CNW networks of (A). Dotted lines are guides for the eye. (C–F) Room temperature AMR curves for the (C) Ni, (D) Ni<sub>75</sub>Co<sub>25</sub>, (E) Ni<sub>32</sub>Co<sub>68</sub>, and (F) Co CNW networks.

toward the observed limiting value for Co networks with perpendicular  $c$ -axis as the Ni content is reduced. It is worth mentioning that the small negative anisotropy contribution observed for the Ni sample could be originated by residual stresses due to the reduced diameter of the NWs, as suggested by de la Torre Medina et al. [48].

Fig. 27.5C–F shows resistance curves measured at 290 K with the external field applied in the OOP and IP directions for interconnected NiCo CNW networks. As observed, the maximum resistance is reached near zero applied field for both directions as the Ni content in the alloy dominates (see Fig. 27.5C and D), which is consistent with remanent magnetization states where the magnetization tends to be aligned along the NW axis, due to shape anisotropy, as suggested in Fig. 27.5A. Conversely, the decrease of the resistance near zero field as the Co content in the alloy is dominant (see Fig. 27.5E and F) is consistent with the decrease of the remanent magnetization (see Fig. 27.5A) as a result of the misalignment of the magnetization with respect to the NWs axis, due to the competing MS and MC anisotropies. The same magnetic behavior was found on the Co-rich  $\text{Ni}_x\text{Co}_{1-x}$  with  $x < 45\%$ . Besides, similar features are observed at temperatures down to 20 K.

Fig. 27.6 shows the AMR ratio versus Ni content ( $x$ ) at  $T = 20, 150,$  and  $290$  K for the different  $\text{Ni}_x\text{Co}_{1-x}$  CNW networks (see [19, 45] for more details on the estimation of AMR ratio in such CNWs). The observed variation of the AMR ratio as a function of  $x$  is consistent with previous reports on electrodeposited films and metallurgically processed NiCo alloys [46, 49, 50], where the maximum at  $x \approx 75\%$  for both temperature values is attributed to a magnetostriction and MC constants close to zero and to a saturation magnetization of about one Bohr magneton per atom for that particular alloy composition [46]. At any temperature, the AMR ratio reported in Fig. 27.6 for  $\text{Ni}_{75}\text{Co}_{25}$  is slightly smaller than the one reported in films and bulk alloy with the same composition. This is due to the larger residual resistivity  $\rho_0$  due to scattering by static lattice defects and surface roughness in CNW structures. Indeed, the residual resistivity ratio ( $\rho_{290\text{K}}/\rho_{20\text{K}}$ ) for the  $\text{Ni}_{75}\text{Co}_{25}$  CNWs sample was only 2.45. Using Matthiessen's rule,  $\rho(T) = \rho_0 + \rho_{\text{e-ph}}(T)$  with  $\rho_{\text{e-ph}}$  the temperature-dependent electron-phonon contribution to the resistivity value of approximately  $8 \mu\Omega\text{cm}$  at RT for this alloy composition [49], we estimated  $\rho_0$  to be around  $5.5 \mu\Omega\text{cm}$  which is about two times greater than the values for films and bulk alloy with the same composition [46, 49, 50]. It should be noticed that the measured electrical resistances of all CNW networks are very stable with time.

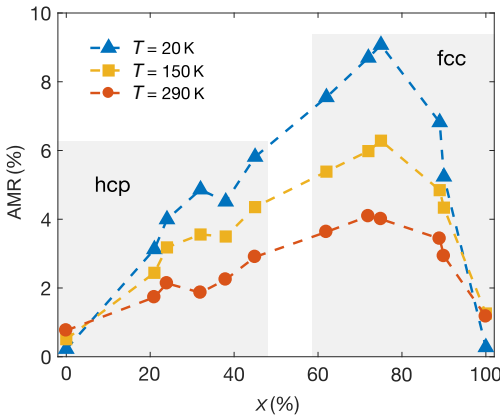


**Fig. 27.6** Variation of the AMR ratio with respect to the Ni content ( $x$ ) at  $T = 20, 150,$  and  $290$  K for the  $\text{Ni}_x\text{Co}_{1-x}$  CNW networks, with  $0 \leq x \leq 1$ .

### 27.3.2 Interconnected Ni NT networks with controlled structural and magnetic properties

In this section, we discuss on the applicability of the electrochemical dealloying method along with the use of track-etched PC membranes with interconnected cylindrical nanopores in order to obtain Ni CNT networks. By using this electrochemical method, magnetic interconnected NT architectures with predefined sizes and shapes and precise spatial control have been obtained. In the first stage of this method, Ni and Cu are co-deposited following a typical chronoamperometric process, which corresponds to the reduction curve displayed in Fig. 27.7A, for a specific potential ( $E = -1.0$  V). This stage leads to a Cu/Ni—core/shell structure as the one displayed schematically in the inset of Fig. 27.7A, showing the phase separation between the two metallic elements. In the second stage of the dealloying method, the Cu cores in the core/shell interconnected network are electrochemically etched by applying an oxidation potential of +0.2 V, as seen in Fig. 27.7B. For this curve, the progressive decrease toward zero of the negative electrical current is the consequence of the decrease of the amount of Cu until its complete dissolution is achieved, leading as a result to a CNT network as shown schematically in the inset of this figure. Besides, based on simple phenomenological arguments, it is possible to propose and validate an expression that states the linear increase for the wall thickness as a function of the diameter of the NTs for a specific electrochemical conditions. The induced structural and morphological changes in the CNTs result in tunable magnetic and magneto-transport properties despite the complex crossed morphology of the networks. In one hand, two main features of the NTs morphology from the control of the electrochemical conditions and

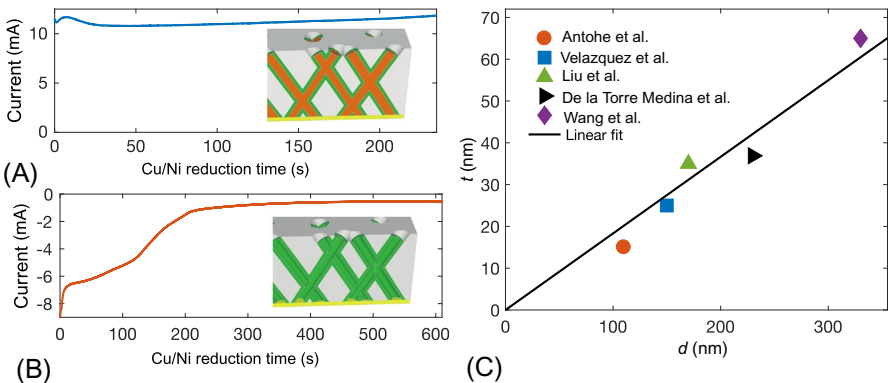


**Fig. 27.7** (A) Reduction and (B) oxidation curves at the respective potentials of  $-1.0$  and  $+0.2$  V in order to obtain an initial core(Cu)/shell(Ni) nanocable network and the successive CNT network into a PC membrane with crossed nanopores. The *insets* show schematic representations of the both crossed nanocable and nanotube networks. (C) Plot of  $t$  versus  $d$  for a Ni CNT network grown at  $E = -1$  V (lozenge) obtained with Eq. (27.1), which is compared to the values reported in the different previous works on parallel NT networks [25, 37–39]. The linear regression is carried out to the whole set of  $t$  versus  $d$  values with a fitting accuracy of 96%.

the host membrane were used for their growth. Specifically, their wall thickness strongly depends on the reduction potential and it is related to their diameter through a linear relationship, that is

$$t = \frac{1}{2}(1 - \sqrt{r})d, \quad (27.1)$$

where  $r = V_{\text{Cu}}/(V_{\text{Cu}} + V_{\text{Ni}})$ , with  $V_{\text{Cu}}$  and  $V_{\text{Ni}}$  the respective Cu core and Ni shell reduced volumes [26]. Eq. (27.1) is a good approximation of the NTs wall thickness since no Ni material is removed during the oxidation stage of the dealloying process. Using Eq. (27.1) with the Ni to Cu volume ratio  $r$  obtained from EDX mappings leads to  $t$ -values that are in very good agreement with those obtained from the electrochemical dealloying procedure. Previous works have also reported different  $t$ -values for NTs of different outer diameters ( $d$ ) in the range from 110 to 330 nm, but made at the same reduction potential ( $E = -1$  V). Plotting the values of  $t$  versus  $d$  from these different previous works and comparing them to the present result for the CNT network fabricated at  $E = -1$  V, corroborates the linear relationship between  $t$  and  $d$ , and the approximate phenomenological expression  $t \approx 0.183 \times d$  is obtained for this reduction potential, as shown in Fig. 27.7C.

On the other hand, the magnetic behavior is analyzed from recorded hysteresis loops at RT with the external field applied in the OOP direction. Fig. 27.8A shows hysteresis loops for four Ni CNT networks with  $t$ -values of 13, 19, 37, and 50 nm. The observed changes in the shape of the hysteresis loops are in good agreement with previous works on arrays of parallel Ni NTs [25, 37]. The decrease of the remanence magnetization for thicker wall thicknesses is attributed to the decrease of the effective magnetic anisotropy. In other words, larger dipolar fields are originated by increasingly closer magnetic charges at the NTs inner surface, whereas lower demagnetizing fields are originated by increasingly more distant magnetic charges in between the NTs inner and outer surfaces. The competition between these fields leads to lower effective magnetic anisotropies that are accompanied by lower remanence magnetization values. This feature is the result of the more rapid increase with  $t$  of the dipolar interaction to demagnetizing field ratio. For the case  $E = -0.8$  V, the magnetic behavior is consistent with the systematic change in shape of the hysteresis loops in Fig. 27.8A. As expected, the remanence increases and the coercive field has almost the same value as those for the other samples. Although the granular feature of NTs makes difficult to elucidate the exact wall thickness from SEM analysis [51], the progressive increase of the remanence magnetization for thinner NTs walls shown in Fig. 27.8A means that the NTs magnetization tends to align along their axis. This feature is consistent with the reduction of the MS effects resulting from the smaller effective packing fraction of the CNT networks [24, 25, 52].

On the other hand, information about the magnetic properties of the distinct CNT networks disregarding magnetization reversal processes can be readily obtained from FMR experiments, as they are carried out in the saturated state. In the present work, only MS contributions are considered because of the polycrystalline nature of the as-obtained NTs using the deposition/dealloying method [51]. This means that the

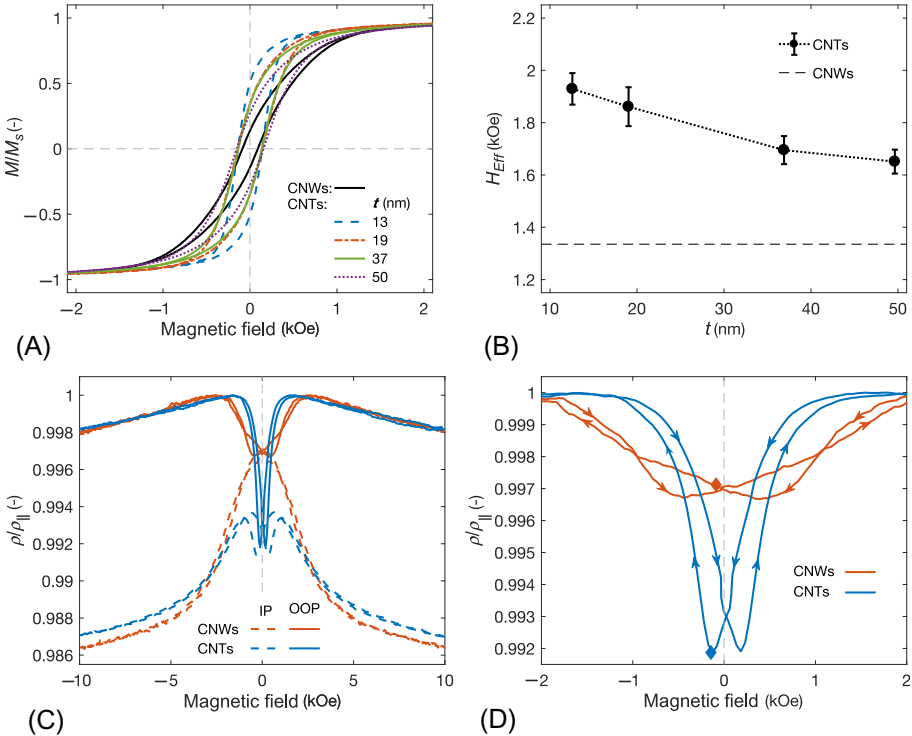


**Fig. 27.8** (A) Hysteresis loops measured with the magnetic field applied along the out-of-plane (OOP) direction of the PC template for Ni CNT networks ( $\phi = 230$  nm) with different wall thicknesses. (B) Variation of  $H_{\text{Eff}}$  as a function of the NTs wall thickness  $t$  (circles) for Ni CNT networks along with the value for a Ni solid CNW network (dash-dotted line). Error bars are estimated from the standard deviation of the corresponding experimental FMR dispersion relations. (C) Anisotropic magneto-resistance curves measured with the external field applied in the OOP (continuous lines) and IP (dashed lines) directions to the plane of the porous template for a CNW and a CNT network with outer diameter of 230 nm. (D) Zoom of the AMR curves in the OOP direction at low fields. The arrows indicate the magnetic field sweep direction from positive to negative or from negative to positive. The lozenges indicate the resistance states at the corresponding coercive field for each network.

magnetic anisotropy is controlled only by changes in the dipolar coupling of the networks via variations of the NTs wall thickness. Fig. 27.8B shows a monotonous decrease of the effective anisotropy field ( $H_{\text{Eff}}$ ) as the NTs wall thickness  $t$  increases. This trend in  $H_{\text{Eff}}$  is consistent with the limiting value for a CNW network embedded in the same porous template, which represents the lower bond for the expected values for CNT networks (dash-dotted line in Fig. 27.8B).

This lower bond is the consequence of the larger competition between the demagnetizing and the dipolar interaction field between NWs, which result from their cylindrical surface charges. In the case of CNT networks, additional surface charges appear at the inner hollow core of the NTs, which lead to a decrease of the dipolar field

and then to an increase of  $H_{\text{Eff}}$ . Indeed, it has been shown that the dipolar field depends on the inner to outer radii ratio  $\beta = r_i/r_e$  [25], such that it tends to zero as  $r_i$  tends to the value of  $r_e$ . Conversely, the dipolar field tends to the maximum value for an array of NWs, as the hollow core disappears. This behavior fairly explains the variation of the effective field with the NTs wall thickness, as observed in Fig. 27.8B. These results are in good agreement with the observed behavior shown in Fig. 27.7C and they help explaining the variation of the remanence magnetization as the NTs wall thickness is modified.

Besides, magneto-transport measurements constitute another way to investigate the magnetic behavior of CNT networks. In this work, AMR is used to obtain a better insight of the magnetic behavior of 3D CNT networks and its key difference with 3D CNW networks. Fig. 27.8C shows measured AMR curves for a CNW network and a CNT network with NWs and NTs diameter of 230 nm and with a NTs inner diameter of 37 nm. Measurements were carried out with the external field applied along the IP (dashed lines) and OOP (continuous lines) directions. From these measurements, AMR ratio of about 1.8% is obtained for both CNW and CNT networks. As expected, these values are very close to each other because the AMR ratio is an intrinsic property of magnetic materials. Moreover, these values are in good agreement with previously reported AMR ratios in arrays of parallel NWs [43]. However, quite different magneto-resistive behavior between CNWs and CNTs appears at low-magnetic fields, as discussed hereafter.

We now turn to the discussion of magnetic states observed in Ni CNTs with the magnetic field applied in the OOP and IP directions. The observed coincidence between the AMR curve minimum in the OOP configuration (see Fig. 27.8D) and the resistance at coercivity for the CNT network means that the total local magnetization within NT segments is close to zero, which in this case coincides with the zero effective magnetization of the entire CNT network observed at the coercive field  $H_c = 144$  Oe in the hysteresis loop. According to the previous works, when the external field is applied at low applied field angles with respect to the NTs axis, the magnetization reversal of NTs is dominated by the curling (vortex) reversal mode, where magnetic moments rotate progressively via propagation of a large number of vortex domain walls [21–23]. Since the AMR curve minimum shown in Fig. 27.8D lies almost at the middle point between the IP and OOP curves, the micromagnetic configuration of the CNTs during magnetization reversal account for a large portion of the moments following the circumference of the NT, thus perpendicular to the current flow, whereas the remaining lie at intermediate orientations between the parallel and antiparallel to the NTs axis. Following the same argument, we attribute the reduction in the resistance curve around  $H_c$  in the IP configuration (Fig. 27.8C) to the creation of vortex domain walls, as previously suggested from AMR experiments carried out on an individual Ni NT [53].

In contrast, the AMR curve minimum for the CNW network does not coincide with the resistance at coercivity (shown as a lozenge). Indeed, starting from the saturated positive state, the resistance minimum for the CNW network is observed at positive field values, in contrast to what is observed in arrays of parallel NWs with only MS contribution to the magnetic anisotropy. In that case, the resistance of the NWs

reaches the minimum value when the direction of the magnetic field is reversed and coincide with the coercive field [42–44]. This effect can be ascribed to the interconnected NW architecture and the presence of domain walls that are formed at the magnetic junctions once the external field is reduced, thus giving rise at low field to complex spin configurations formed by a series of domains in the axially saturate states separated by domains walls at the segment intersections. As may be expected, the junction volume has distinct effects on the domain wall configuration and the initial magnetic switching.

## 27.4 NW network-based spin caloritronics

### 27.4.1 Spin-dependent thermoelectric transport in multilayered NW networks

The diffusion thermopower arises from a diffusion of charge carriers opposite to the temperature gradient. It is related to the energy-dependent conductivity of the material  $\sigma(\epsilon)$  by Mott's formula:

$$S = -eL_0T \left( \frac{d \ln \sigma(\epsilon)}{d\epsilon} \right) \Big|_{\epsilon=\epsilon_F}, \quad (27.2)$$

with  $L_0 = 2.44 \times 10^{-8} \text{ V}^2 \text{ K}^{-2}$  is the Lorenz number and  $e$  is the electron charge (positive). According to Einstein's relation for a metal or alloy with isotropic properties, the conductivity is proportional to the density of states  $\mathcal{N}(\epsilon)$  and to the scattering time  $\tau(\epsilon)$ , where both terms in Eq. (27.2) are to be evaluated at the Fermi level  $\epsilon_F$ . Because of the pronounced structure of the d-band and the high energy derivative of the density of states at the Fermi level in 3d ferromagnetic metals, large diffusion thermopowers are obtained (e.g.,  $S \approx -30 \mu\text{V K}^{-1}$  in cobalt at RT). Also, these magnetic metals exhibit significant magnon-drag contribution to the thermoelectric power within a wide temperature range [54, 55]. Besides, the largest RT thermoelectric power factor ( $\text{PF} = S^2\sigma$ , with  $\sigma$  the electrical conductivity), which is the physical parameter that relates to the output power density of a thermoelectric material, is achieved for Co ( $\text{PF} \approx 15 \text{ mW K}^{-2} \text{ m}$ ) [56].

In FM/Cu multilayered NWs (see Fig. 27.9A), the Seebeck coefficient along the axial direction (perpendicular direction to the layers) can be calculated from the corresponding transport properties using Kirchhoff's rules [57]

$$S_{\perp} = \frac{S_{\text{Cu}}\kappa_{\text{FM}} + \lambda S_{\text{FM}}\kappa_{\text{Cu}}}{\lambda\kappa_{\text{Cu}} + \kappa_{\text{FM}}} \quad (27.3)$$

Here  $S_{\text{FM,Cu}}$  and  $\kappa_{\text{FM,Cu}}$  represent the thermopower and the thermal conductivity of the FM and Cu metals and  $\lambda = t_{\text{FM}}/t_{\text{Cu}}$  the thickness ratio of FM and Cu layers. In metals, heat conductivity is primarily due to free electrons. The Wiedemann-Franz law states that the ratio of thermal conductivity and electrical conductivity  $\sigma$  for metals fairly

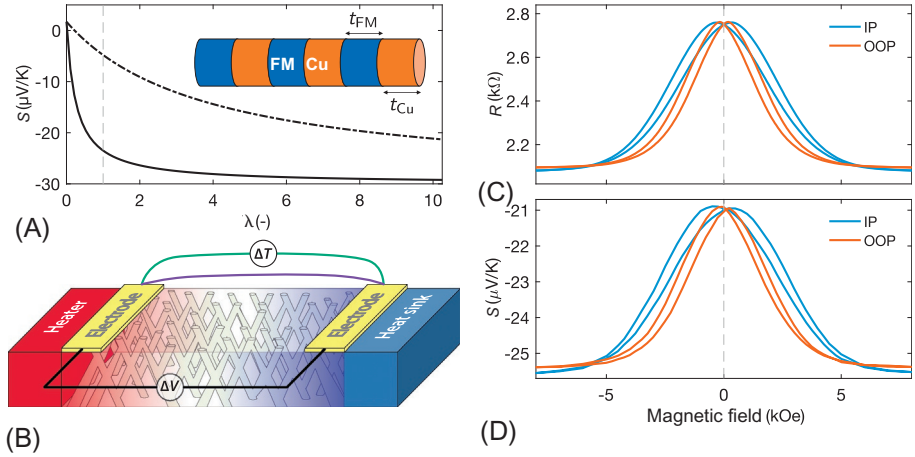


**Fig. 27.9** (A) Calculated thermopower for Co/Cu multilayers in the layer parallel (*dash-dotted line*) and perpendicular (*solid line*) directions versus thickness ratio  $\lambda = t_{\text{FM}}/t_{\text{Cu}}$  using Eqs. (27.4), (27.5) and bulk values for  $S_{\text{Co}}$ ,  $\rho_{\text{Co}}$ ,  $S_{\text{Cu}}$ , and  $\rho_{\text{Cu}}$ . The *gray-dashed line* shows the values for  $\lambda = 1$ . The *inset* shows an FM/Cu multilayer stack. (B) Experimental set-up for Seebeck coefficient and the magneto-thermoelectric effect measurements. Device dimensions are 15 mm long, 5 mm wide, and 22  $\mu\text{m}$  thick and the *color* represents the generated temperature profile in the NW networks. The gold electrodes are 2 mm wide. (C and D) Electrical resistance (C) and Seebeck coefficient (D) of a Co/Cu NW network 80 nm in diameter and 3% packing density showing similar magnetic field dependence corresponding to  $\text{MR} = 24.7\%$  and  $\text{MTP} = -22.3\%$  at room temperature. The *curves* in (C and D) were obtained with the applied field in-plane (IP—in *blue*) and out-of-plane (OOP—in *red*) of the NW network film.

accurately obeys  $\kappa/\sigma = LT$ , where  $T$  is the temperature and  $L$  is the Lorenz ratio. Therefore, considering multilayer stacks made of Cu and ferromagnetic metals, Eq. (27.3) simply reduces to

$$S_{\perp} = \frac{S_{\text{Cu}}\rho_{\text{Cu}} + \lambda S_{\text{FM}}\rho_{\text{FM}}}{\lambda\rho_{\text{FM}} + \rho_{\text{Cu}}} \quad (27.4)$$

with  $\rho_{\text{FM}}$  and  $\rho_{\text{Cu}}$  the corresponding electrical resistivities. According to Eq. (27.4),  $S_{\text{FM}/\text{Cu}}$  is mainly determined by the large thermopower of the FM metal in case the thickness ratio  $\lambda$  is not too small since  $S_{\text{FM}}\rho_{\text{FM}} \gg S_{\text{Cu}}\rho_{\text{Cu}}$ . The same conclusion is drawn when the FM layer is formed from alloys such as CoNi and NiFe because of highly contrasting thermal conductivity values between the alloy and Cu. In contrast, the Seebeck coefficient of a planar FM/Cu multilayer stack in the direction parallel to the layers is given by

$$S_{\parallel} = \frac{S_{\text{Cu}}\rho_{\text{FM}} + \lambda S_{\text{FM}}\rho_{\text{Cu}}}{\lambda\rho_{\text{Cu}} + \rho_{\text{FM}}} \quad (27.5)$$

showing that large thermopower can be obtained only if the thickness ratio  $\lambda$  is very large. The contrasting behavior between layer parallel and perpendicular directions is illustrated in Fig. 27.9A for Co/Cu multilayers from the bulk resistivity and thermopower values at RTe. So, these multilayered NW networks with alternate stacks of dissimilar materials such as a ferromagnetic metal or alloy and a noble metal are promising candidates for good thermoelectric materials.

In this section, we report on experimental results obtained in custom-fabricated spin caloritronic devices based on FM/Cu CNWs with FM = Co or equiatomic CoNi alloy. In such centimeter-scale NW networks, electrical connectivity is essential to allow charge flow over the whole sample sizes. Besides, the branched NW architecture enables electrical measurement in the CPP geometry. For conducting magneto-transport measurements, the cathode was locally removed by plasma etching to create a two-probe design suitable for electric measurements, with the flow of current restricted along the NW segments, thus perpendicularly to the plane of the layers. The device configuration to measure the Seebeck coefficient and the magneto-thermoelectric effect is schematically represented in Fig. 27.9B. Heat flow is generated by a resistive element and a thermoelectric voltage  $\Delta V$  is created by the temperature difference  $\Delta T$  between the two metallic electrodes that is measured by a thermocouple (see [35] for details).

As shown in Fig. 27.9C and D, the resistance and thermopower of the low-packing density ( $P = 3\%$ ) Co/Cu NW sample show the same magnetic field dependencies and similar relative changes of  $\sim 25\%$  at  $H = 8$  kOe at RT. The samples are nearly magnetically isotropic, as observed from the magneto-transport curves obtained with the applied magnetic field along the OOP and IP directions of the NW network films (see Fig. 27.9C and D). This behavior corresponds to the one expected considering the CNW architecture and MS arguments when using similar magnetic and nonmagnetic layer thicknesses [58]. In the following, only the measurements obtained in the plane of the CNW network films are reported. The crossed Co/Cu NW networks were found to exhibit very large GMR responses (defined as  $GMR = R_{AP}/R_P - 1$ , with  $R_{AP}$  and  $R_P$  the corresponding resistances in the high- and low-resistance states, respectively) reaching values of 33% at RT and 58% at  $T = 10$  K in the present study. The same features were observed on the CoNi/Cu CNW samples in which GMR effects up to 86% were obtained at low temperatures. Besides, the measured RT thermopower on the Co/Cu NW network in the saturated state ( $S \approx -25.5 \mu\text{V K}^{-1}$ ) is only slightly smaller than the value found in pure cobalt material.

The absolute value of the magnetothermopower,  $MTP = (S_{AP} - S_P)/S_{AP}$ , with  $S_{AP}$  and  $S_P$  the corresponding thermopowers in the high- and low-resistance states, respectively, shows a similar increase with decreasing temperature as the MR ratio (defined as  $MR = (R_{AP} - R_P)/R_{AP}$ ) in the temperature range near RT (see Fig. 27.10A). However, in the low-temperature range, the MTP exhibits a less pronounced effect. Recent estimations of the thermoelectric PF at RT for both Co/Cu and CoNi/Cu CNW networks lead to values around  $7.5 \text{ mW K}^{-2} \text{ m}$  in the saturated state [35, 36], which are larger than the PF of the widely used thermoelectric material, bismuth telluride (in the range  $1\text{--}5 \text{ mW K}^{-2} \text{ m}$ ) [59]. Besides, the PF values obtained for FM/Cu NW networks embedded in polymer membranes are at least one order of magnitude

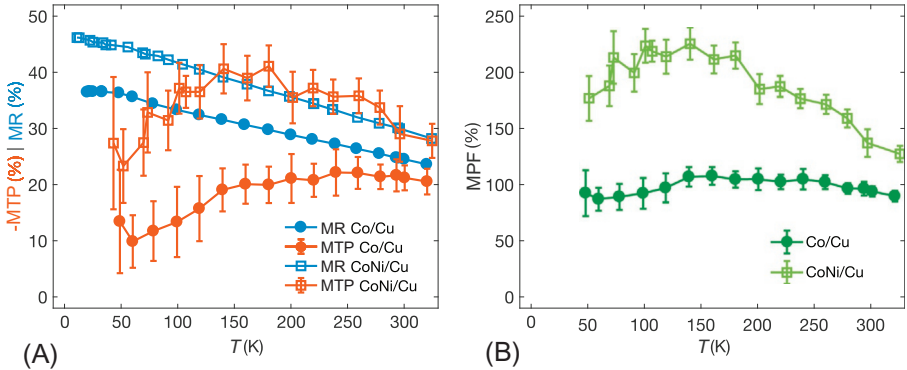


**Fig. 27.10** (A) MR ratio and MTP as a function of temperature with the field applied in the plane of the Co/Cu (*full circles*) and CoNi/Cu (*empty squares*) NW network films. (B) Magneto-power factor as a function of temperature obtained using the MR and MTP data in (A). The error bars in (A) and (B) reflect the uncertainty of the electrical and temperature measurements and is set to two times the standard deviation, gathering 95% of the data variation.

larger than those of flexible thermoelectric films based on optimized conducting polymers, namely PEDOT-Tos films [60]. The magneto-power factor ( $MPF = (PF_P - PF_{AP})/PF_{AP}$ ) can be expressed as  $MPF = (1 - MTP)^2 / (1 - MR) - 1$ . For the Co/Cu CNWs, the values reach  $\sim 100\%$  at RT and show a weak temperature variation down to  $T \approx 50$  K (see Fig. 27.10B). In contrast, the MPF for the CoNi/Cu CNWs increases with decreasing temperature and exceeds 200% at  $T = 150$  K, as also shown in Fig. 27.10B. The efficiency of a material's thermoelectric energy conversion is determined by its figure of merit  $ZT = S^2\sigma T/\kappa$ , with  $\kappa$  the thermal conductivity. In a previous work, Ou et al. [61] have measured the thermal conductivity of a suspended nickel NW for  $T = 15\text{--}300$  K. While the Lorenz ratio  $L = \kappa/\sigma T$  departs from the Sommerfeld value ( $L_0 = 2.45 \times 10^{-8} \text{ V}^2 \text{ K}^{-2}$ ) at low temperatures,  $L$  was found to be equal to  $L_0$  with a 5% margin of error above  $T = 50$  K. Due to the very low thermal conductivity of PC ( $\kappa = 0.2 \text{ W m}^{-1} \text{ K}$  at RT), the contribution of the polymer matrix to heat transport is much smaller than that of the metallic NW network. Indeed, assuming that the Wiedemann-Franz law holds for Co/Cu (CoNi/Cu) NWs, an estimate of the RT electronic thermal conductivity gives  $\kappa_E = 63 \text{ W m}^{-1} \text{ K}$  ( $\kappa_E = 50 \text{ W m}^{-1} \text{ K}$ ) for an AP configuration and  $\kappa_E = 84 \text{ W m}^{-1} \text{ K}$  ( $\kappa_E = 72 \text{ W m}^{-1} \text{ K}$ ) for a P configuration. In this case, the figure of merit is reduced to  $ZT = S^2/L_0$ , thus leading to  $ZT \approx 2.5 \times 10^{-2}$  ( $ZT \approx 3.1 \times 10^{-2}$ ) for the Co/Cu (CoNi/Cu) NW network sample at RT [35, 36]. Although the figure of merit is more than one order of magnitude smaller than those of state-of-the-art thermoelectric materials ( $ZT \approx 1$  in BiTe alloys), it is comparable to those of thermocouple alloys ( $ZT \approx 6 \times 10^{-2}$  and  $ZT \approx 1.4 \times 10^{-2}$  in constantan and chromel, respectively) and can be used in applications for devices with low energy requirements when the supply of heat essentially is free as with waste heat. Furthermore, considering the energy conversion from heat to electric power, the  $ZT$  of the proposed device is much larger than that of a spin Seebeck power generator

( $ZT \approx 10^{-4}$ ) based on a device using a two-step conversion process and the inverse spin Hall effect to convert spin current to charge current in nonmagnetic materials [62].

In the limit of no-spin relaxation, most of the CPP-GMR data can be understood using a simple two-current series-resistor model, in which the resistance of layers and interfaces simply add and where “up” and “down” charge carriers are propagating independently in two spin channels with large spin asymmetries of the electron’s scattering [63, 64]. Similarly, significantly different Seebeck coefficients for spin-up and spin-down electrons,  $S_{\uparrow}$  and  $S_{\downarrow}$ , are expected because the d-band is exchange-split in these ferromagnets, as suggested from previous works performed on dilute magnetic alloys [65, 66]. Assuming that the layers of the magnetic multilayers are thin compared to the spin-diffusion lengths and according to the usual rule when the currents split to flow along two parallel paths (see Fig. 27.11A), the corresponding thermopowers  $S_{AP}$  and  $S_P$  are simply given by [67]

$$S_{AP} = \frac{S_{\uparrow}\rho_{\uparrow} + S_{\downarrow}\rho_{\downarrow}}{\rho_{\uparrow} + \rho_{\downarrow}} \quad (27.6)$$

and

$$S_P = \frac{S_{\uparrow}\rho_{\downarrow} + S_{\downarrow}\rho_{\uparrow}}{\rho_{\uparrow} + \rho_{\downarrow}}, \quad (27.7)$$

where separate resistivities  $\rho_{\uparrow}$  and  $\rho_{\downarrow}$  and Seebeck coefficients  $S_{\uparrow}$  and  $S_{\downarrow}$  are defined for majority and minority spin channels. Therefore, the spin-dependent Seebeck coefficients,  $S_{\uparrow}$  and  $S_{\downarrow}$ , can be expressed as follows:

$$S_{\uparrow} = \frac{1}{2} [S_{AP}(1 - \beta^{-1}) + S_P(1 + \beta^{-1})], \quad (27.8)$$

$$S_{\downarrow} = \frac{1}{2} [S_{AP}(1 + \beta^{-1}) + S_P(1 - \beta^{-1})], \quad (27.9)$$

where  $\beta = (\rho_{\downarrow} - \rho_{\uparrow})/(\rho_{\downarrow} + \rho_{\uparrow})$  denotes the spin asymmetry coefficient for resistivity. From Eqs. (27.8), (27.9), it can be easily deduced that  $S_{\uparrow} = S_P$  and  $S_{\downarrow} = S_{AP}$  in the limit of an extremely large MR ratio ( $\beta \rightarrow 1$ ). The temperature evolutions of  $S_{AP}$ ,  $S_P$ ,  $S_{\uparrow}$ , and  $S_{\downarrow}$  are shown in Fig. 27.11B and C.

For both Co/Cu and CoNi/Cu CNWs, the Seebeck coefficients decrease almost linearly with decreasing temperature, which is indicative of the dominance of diffusion thermopower. The estimated values at RT of MR, MTP,  $PF_P$ , MPF,  $S_{\uparrow}$ , and  $S_{\downarrow}$  are reported in Table 27.2, using  $\beta = MR^{1/2}$  in Eqs. (27.8), (27.9). The values of  $S_{\uparrow}$  and  $S_{\downarrow}$  for Co/Cu CNWs are similar to those previously reported in bulk Co ( $S_{\uparrow} = -30 \mu V K^{-1}$  and  $S_{\downarrow} = -12 \mu V K^{-1}$ ) [66]. Also, the value of  $\beta$  so obtained for Co/Cu CNWs ( $\beta \approx 0.5$ ) is in agreement with previous estimates from the CPP-GMR experiments carried out on Co/Cu multilayers [64]. In contrast, our value for  $\Delta S = S_{\uparrow} - S_{\downarrow}$  of  $-9.4 \mu V K^{-1}$  and  $-11.5 \mu V K^{-1}$  for Co/Cu and CoNi/Cu CNWs,

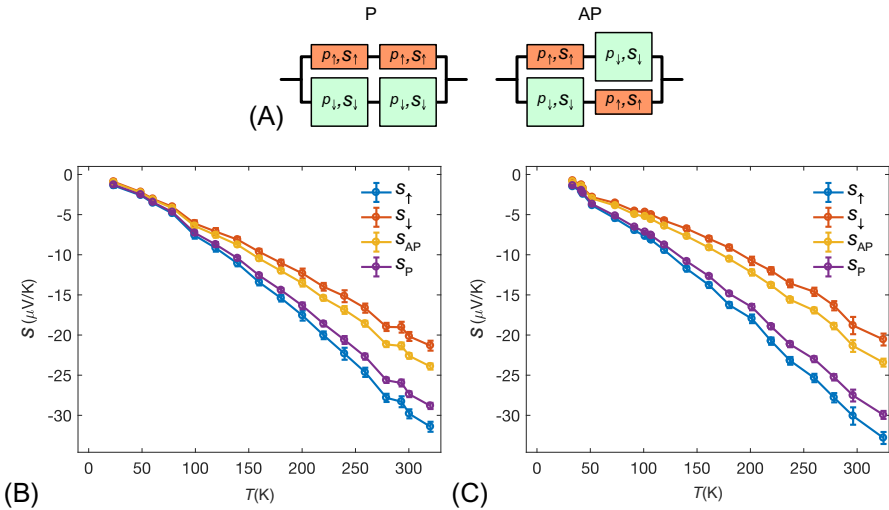


**Fig. 27.11** (A) The two-current model for the resistivity and the thermopower considering both parallel (P) and antiparallel (AP) magnetic configurations. (B, C) Measured Seebeck coefficients at zero applied field  $S_{AP}$  (orange circles) and at saturating magnetic field  $S_P$  (violet circles) of (B) a Co/Cu and (C) a CoNi/Cu NW network 80 nm in diameter and 3% packing density, along with the corresponding calculated  $S_{\uparrow}$  (blue circles) and  $S_{\downarrow}$  (red circles) from Eqs. (27.8), (27.9) (see text). The error bars reflect the uncertainty of the electrical and temperature measurements and is set to two times the standard deviation, gathering 95% of the data variation.

respectively, are much larger than the one of  $-1.8 \mu\text{V K}^{-1}$  extracted from measurements performed on Co/Cu/Co nanopillar spin valve using a 3D finite-element model [32, 68].

Since the magnetothermopower can also be expressed as  $MTP = 2\beta\eta/(1 + \beta\eta)$ , where  $\eta = (S_{\downarrow} - S_{\uparrow})/(S_{\downarrow} + S_{\uparrow})$  denotes the spin asymmetry for Seebeck coefficients, infinitely large MTP and MPF effects are expected when the product  $\beta\eta$  tends to  $-1$ . In previous works performed using ferromagnetic dilute alloys with the occurrence of a virtual bound state at the Fermi level [65, 66],  $S_{\uparrow}$  and  $S_{\downarrow}$  were found to have an opposite sign, which corresponds to  $|\eta| > 1$ . Therefore, the fabrication of

**Table 27.2** Room temperature data of the Co/Cu and CoNi/Cu nanowire networks.

	MR (%)	MTP (%)	PF <sub>P</sub> (mW K <sup>-2</sup> m)	MPF (%)	$S_{\uparrow}$ ( $\mu\text{V K}^{-1}$ )	$S_{\downarrow}$ ( $\mu\text{V K}^{-1}$ )
Co/Cu	24.7	-22.3	7.5	99	-28.0	-18.5
CoNi/Cu	30.2	-29.3	7.5	135	-30.2	-18.7

multilayered NWs with appropriate magnetic layer composition should make it possible to fine-tune the PF of thermoelectric energy conversion with an external magnetic field.

Further evidence that the thermopower is dominated by electron diffusion over the whole temperature range investigated is presented in Fig. 27.12A and B. Defining the diffusion thermopower  $S(H) = eL_0T\rho'(H)/\rho(H)$  by Mott's formula (Eq. 27.2) with  $\rho'(H) = (d\rho(H)/d\epsilon)_{\epsilon=\epsilon_F}$  the derivative of the electrical resistivity with respect to the energy, evaluated at the Fermi level, one can write  $S_{AP} = eL_0T\rho'_{AP}/\rho_{AP}$  and  $S_P = eL_0T\rho'_P/\rho_P$ . Then, the following expression describing the inverse relationship between the field-dependent thermopower and electrical resistance can be easily obtained:

$$S(H) = A + \frac{B}{R(H)}, \quad (27.10)$$

where  $A = (S_P R_P - S_{AP} R_{AP}) / (R_P - R_{AP})$  and  $B = (R_P R_{AP} (S_{AP} - S_P)) / (R_P - R_{AP})$ . This expression corresponds to an equivalent form of the Gorter-Nordheim relation for diffusion thermopower in metals and alloys [54] and has been observed at different temperatures in the interconnected network made of Co/Cu and CoNi/Cu NWs, as shown in Fig. 27.12A and B.

#### 27.4.2 Magnetic control in heat management

Current flow in the high-packing density Co/Cu NW sample ( $P = 20\%$ ) results in Joule heating as well as a Peltier heat current at the junctions between the NW network and the gold electrode, as shown in Fig. 27.13A. These heat flows were monitored continuously from the temperature changes using a highly sensitive Cernox thermometer ( $<3$  mg,  $1$  mm<sup>2</sup>; Cernox-1010, Lake Shore Cryotronics Inc., OH, United States) with respect to the operating temperatures for different current intensities and polarities, as well as for various applied magnetic fields. Net cooling occurs at low currents when the direction of the Peltier heat current flow is such that  $\Pi I < 0$  at the considered junction (with  $\Pi$ , the Peltier coefficient) and dominates over the Joule heating effect ( $RI^2$ ), as shown in Fig. 27.13B. In this case, when the DC current flows from the NWs (with the higher Peltier coefficient) to the gold electrode (with the lower one), the Peltier heat is released from the junction, that is, net cooling happens (see Fig. 27.13B). As expected, the situation is reversed when the current flows in the opposite direction. For higher currents, the Joule heating dominates over the Peltier cooling, as shown in the inset of Fig. 27.13C by temperature versus time traces for  $I = \pm 50$  mA. Unlike the Peltier effect that leads to a cooling or a heating of the system depending on the direction of current flow, the Joule effect does not depend on the current polarity. It is thus possible to separate the two effects linearly [36]. From the inset of Fig. 27.13C, one can estimate the Peltier cooling ability of Co/Cu CNW network of  $\sim 8.5$  K A<sup>-1</sup>.

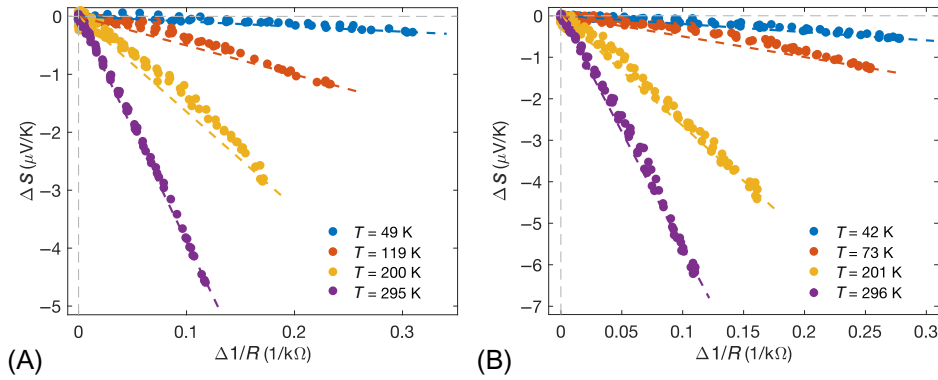


**Fig. 27.12** Linear variation of  $\Delta S(H)$  versus  $\Delta(1/R(H))$  at different measured temperatures illustrating the Gorter-Nordheim characteristics for (A) a Co/Cu and (B) a CoNi/Cu NW network 80 nm in diameter and 3% packing density. The *solid lines* correspond to the theoretical relation shown in Eq. (27.10) (see text).

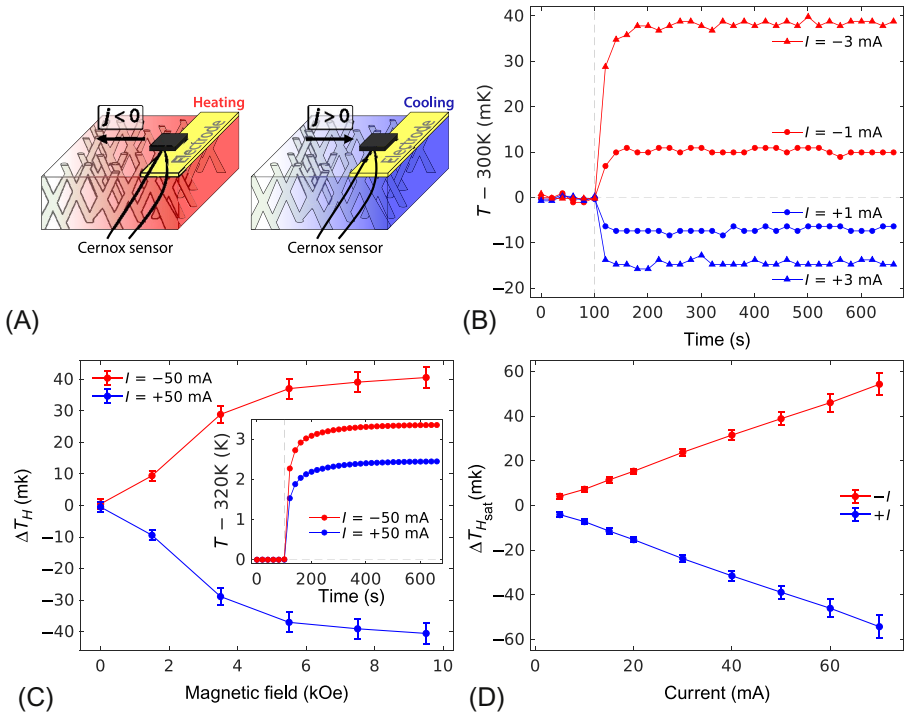


**Fig. 27.13** (A) Schematics of a set-up for direct observation of Peltier and magneto-Peltier effects. (B) Temperature versus time traces of the sum of the Joule and Peltier heats relative to a working temperature of 300 K. The direct currents are switched on after 100 s as shown by the vertical dashed lines and are applied both forward and reverse in the interconnected Co/Cu nanowires of 105 nm in diameter and with a packing density of 22% ( $R = 3.3 \Omega$ ,  $MR = 12\%$ ). (C) Measured temperature changes  $\Delta T_H$  at the Peltier junction during the magnetic field sweep for a DC current of  $-50$  and  $+50$  mA. Here, the contribution from the Peltier heating has been estimated using a procedure described elsewhere [35, 36]. The Peltier term leads to heating and cooling at the saturation field of 9.5 kOe and depends on current flow direction. The inset shows the same as in (B) but for higher current intensities for which the Peltier effect becomes dominated by the Joule heating. (D) Measured total temperature changes  $\Delta T_{H,\text{sat}}$  at the Peltier junction between the zero field ( $T_{H_0}$ ) and saturated states ( $T_{H,\text{sat}}$ ) versus current intensity applied both forward and reverse. The error bars in (C) and (D) reflect the uncertainty of the temperature measurements and is set to two times the standard deviation, gathering 95% of the data variation.

As shown in Fig. 27.13C, the magneto-Peltier effect has been quantified by recording the temperature change  $\Delta T_H$  during the magnetic field sweeps. The field dependence of  $\Delta T_H$  resembles to that of MR. The same measurements were performed for different currents, as shown in Fig. 27.13D where the total temperature change ( $\Delta T_{H,\text{sat}} = T_{H_0} - T_{H,\text{sat}}$ ) between the zero field ( $T_{H_0}$ ) and saturation ( $T_{H,\text{sat}}$ ) states is reported. As expected, the magneto-Peltier effect increases linearly with the driving current. From these results, one can obtain the guideline for the magnitude of the magnetically controlled cooling and heating ability of a macroscopic electronic

component against the injected current. Using the values of  $S_{\uparrow}$  and  $S_{\downarrow}$  from Fig. 27.11B and the Onsager relation which relates the two thermoelectric coefficients  $\Pi = ST$ , one may estimate the maximum difference between the Peltier coefficients in the AP and P states for an infinite MR ratio as  $\Pi_{\uparrow} - \Pi_{\downarrow}$ , which correspond to  $-2.8$  mV at RT for Co/Cu NWs. Since currents up to few hundreds mA are able to pass through the densely packed NW films without damaging the network structure, we may anticipate that a magnetic field can switch a heat flow as large as 1 mW.

## 27.5 Conclusion and future perspectives

The present 3D networks of magnetic NWs and NTs are of special interest due to their potential for memory devices, computing architectures, sensing, and biomedical applications. Among the advantages of the interconnected NW architecture are its mechanically stable and self-supporting feature after chemical dissolution of the polymer membrane, as well as the ease of carrying out magneto-transport measurements.

In this chapter, we have explored the interplay between the magnetic and magneto-transport properties of 3D NW networks made of various magnetic metals and alloys. The close relationship between their magnetic and structural properties has a direct impact on their magneto-transport behavior. Control of the electrodeposition conditions, in particular, the electrolytic bath acidity made possible to modify the crystallographic structure of Co CNW networks, which strongly influenced its magnetic anisotropy, microwave absorption, and anisotropic magneto-resistance. The feasibility to obtain considerable AMR signals, being stable overtime, in CoNi CNW networks made them very interesting structures for their use as magnetic sensors. In addition, we explored the fabrication and the corresponding magnetic and magneto-transport behavior of a complex nano-architecture based on CNT networks. We have shown that Ni CNT networks with controlled wall thickness (in the range 10–100 nm) can be obtained using appropriate reduction or deposition potential of the crossed core(Cu)/shell(Ni) nanocables. Again, the excellent control over geometrical parameters and morphological features of the Ni CNT networks leads to tunable magnetic and magneto-transport properties. Particularly, the low field magneto-transport behavior is consistent with the expected vortex-like states formed in different segments of the NT scaffold.

On the other hand, embedded NW networks in porous polymer films are also perspective materials for spin caloritronics applications. So far, major experimental issues are the insufficient power generation capability in magnetic nanostructures (such as spin valve nanopillars and magnetic tunnel junctions) given the sub-micrometer lateral dimensions and the lack of established methods for reliable measurements of spin caloritronic material parameters. In this chapter, the fabrication of centimeter-scale interconnected network films made of multilayered NWs showing GMR and giant magneto-thermoelectric effects are reported. The 3D NW networks provide promise for flexible thermogenerators that cannot be considered with conducting polymers because of their relatively poor thermoelectric performance and with widely used inorganic thermoelectric semiconductors such as bismuth telluride

(Bi<sub>2</sub>Te<sub>3</sub>)-based alloys, as they are both brittle and expensive. In contrast, this work has allowed us to demonstrate extremely large and magnetically modulated thermoelectric PF up to 7.5 mW K<sup>-2</sup>, which is a factor of 2–5 larger than that of (Bi<sub>2</sub>Te<sub>3</sub>)-based alloys and at least one order of magnitude larger than those of optimized conducting polymers. These macroscopic NW networks have enabled us to obtain the magnetic field control of Peltier cooling of macroscopic electronic components and to directly extract key material parameters for spin caloritronics such as spin-dependent Seebeck and Peltier coefficients.

Our work provides a simple and cost-effective pathway to fabricate highly efficient and large-scale NW-based thermoelectric films meeting key requirements for electrical, thermal, and mechanical stability. In addition, since there is no sample size limitation, this fabrication method is expandable into network films with much larger dimensions. A practical thermoelectric cooler made of flexible and shapeable thermoelectric modules consisting of stacked NW network films that are connected electrically in series and thermally in parallel can be easily obtained. With this, we radically change the background of the burgeoning field of spin caloritronics and open an exciting and a promising pathway for the next generation of flexible and light weight thermoelectric devices exploiting the spin degree of freedom and the realization of magnetic thermal switch for heat management. Besides, our flexible thermoelectric films based on macroscopic 3D interconnected NW networks can also be used in applications for devices with low energy requirements when the supply of heat essentially is free as with waste heat.

To sum up, this chapter opens up the possibility for a controlled template-assisted synthesis of complex NW-based architectures with an excellent control over geometrical features, morphology, and chemical composition, leading to tunable magnetic, magneto-transport, and thermoelectric properties.

## Acknowledgments

Financial support was provided by the Belgian Fund for Scientific Research (FNRS). Tristan da Câmara Santa Clara Gomes is a Research Fellow of the FNRS. Flavio Abreu Araujo is a Post-doctoral Researcher of the FNRS. Joaquín de la Torre Medina thanks the UNAM-PAPIIT IN106619 for financial support. The authors would like to thank Dr. E. Ferain and the it4ip Company for supplying PC membranes.

## References

- [1] W. Wang, M. Tian, A. Abdulagatov, S.M. George, Y.-C. Lee, R. Yang, Three-dimensional Ni/TiO<sub>2</sub> nanowire network for high areal capacity lithium ion microbattery applications, *Nano Lett.* 12 (2) (2012) 655–660, <https://doi.org/10.1021/nl203434g>.
- [2] C. Wei, H. Pang, B. Zhang, Q. Lu, S. Liang, F. Gao, Two-dimensional β-MnO<sub>2</sub> nanowire network with enhanced electrochemical capacitance, *Sci. Rep.* 3 (2013) 2193 EP, <https://doi.org/10.1038/srep02193>.
- [3] A. Vlad, V.-A. Antohe, J.M. Martinez-Huerta, E. Ferain, J.-F. Gohy, L. Piraux, Three-dimensional interconnected Ni<sub>core</sub> NiO<sub>shell</sub> nanowire networks for lithium microbattery architectures, *J. Mater. Chem. A* 4 (2016) 1603–1607, <https://doi.org/10.1038/srep02193>.

- [4] O.S. Kwon, S.J. Park, H. Yoon, J. Jang, Highly sensitive and selective chemiresistive sensors based on multidimensional polypyrrole nanotubes, *Chem. Commun.* 48 (2012) 10526–10528, <https://doi.org/10.1038/srep02193>.
- [5] L. Piraux, V.-A. Antohe, E. Ferain, D. Lahem, Self-supported three-dimensionally interconnected polypyrrole nanotubes and nanowires for highly sensitive chemiresistive gas sensing, *RSC Adv.* 6 (2016) 21808–21813, <https://doi.org/10.1039/C6RA03439J>.
- [6] P. Ingo, V. Hrkac, S. Kaps, V. Cretu, O. Lupan, T. Braniste, V. Duppel, I. Tiginyanu, L. Kienle, R. Adelung, Y.K. Mishra, Three-dimensional SnO<sub>2</sub> nanowire networks for multifunctional applications: from high-temperature stretchable ceramics to ultrasensitive sensors, *Adv. Electron. Mater.* 1 (8) (2015) 1500081, <https://doi.org/10.1002/aelm.201500081>.
- [7] M. Rauber, I. Alber, S. Müller, R. Neumann, O. Picht, C. Roth, A. Schökel, M.E. Toimil-Molares, W. Ensinger, Highly-ordered supportless three-dimensional nanowire networks with tunable complexity and interwire connectivity for device integration, *Nano Lett.* 11 (6) (2011) 2304–2310, <https://doi.org/10.1021/nl2005516>.
- [8] M.R.J. Scherer, U. Steiner, Efficient electrochromic devices made from 3D nanotubular gyroid networks, *Nano Lett.* 13 (7) (2013) 3005–3010, <https://doi.org/10.1021/nl303833h>.
- [9] E.J.W. Crossland, M. Kamperman, M. Nedelcu, C. Ducati, U. Wiesner, D.M. Smilgies, G.E.S. Toombes, M.A. Hillmyer, S. Ludwigs, U. Steiner, H.J. Snaith, A bicontinuous double gyroid hybrid solar cell, *Nano Lett.* 9 (8) (2009) 2807–2812, <https://doi.org/10.1021/nl803174p>.
- [10] S. Wang, L.-P. Xu, H.-W. Liang, S.-H. Yu, Y. Wen, S. Wang, X. Zhang, Self-interconnecting Pt nanowire network electrode for electrochemical amperometric biosensor, *Nanoscale* 7 (2015) 11460–11467, <https://doi.org/10.1039/C5NR02526E>.
- [11] S. Rahong, T. Yasui, T. Yanagida, K. Nagashima, M. Kanai, A. Klamchuen, G. Meng, Y. He, F. Zhuge, N. Kaji, T. Kawai, Y. Baba, Ultrafast and wide range analysis of DNA molecules using rigid network structure of solid nanowires, *Sci. Rep.* 4 (2014) 5252 EP, <https://doi.org/10.1038/srep05252>.
- [12] S. Rahong, T. Yasui, T. Yanagida, K. Nagashima, M. Kanai, G. Meng, Y. He, F. Zhuge, N. Kaji, T. Kawai, Y. Baba, Three-dimensional nanowire structures for ultra-fast separation of DNA, protein and RNA molecules, *Sci. Rep.* 5 (2015) 10584 EP, <https://doi.org/10.1038/srep10584>.
- [13] D. Wang, H.P. Jakobson, R. Kou, J. Tang, R.Z. Fineman, D. Yu, Y. Lu, Metal and semiconductor nanowire network thin films with hierarchical pore structures, *Chem. Mater.* 18 (18) (2006) 4231–4237, <https://doi.org/10.1021/cm052216b>.
- [14] M. Tian, W. Wang, Y. Wei, R. Yang, Stable high areal capacity lithium-ion battery anodes based on three-dimensional Ni-Sn nanowire networks, *J. Power Sources* 211 (2012) 46–51, <https://doi.org/10.1016/j.jpowsour.2012.03.084>.
- [15] J. Martín, M. Martín-González, J. Francisco Fernández, O. Caballero-Calero, Ordered three-dimensional interconnected nanoarchitectures in anodic porous alumina, *Nat. Commun.* 5 (2014) 5130 EP, <https://doi.org/10.1038/ncomms6130>.
- [16] E. Araujo, A. Encinas, Y. Velázquez-Galván, J.M. Martínez-Huerta, G. Hamoir, E. Ferain, L. Piraux, Artificially modified magnetic anisotropy in interconnected nanowire networks, *Nanoscale* 7 (4) (2015) 1485–1490, <https://doi.org/10.1039/C4NR04800H>.
- [17] E. Ferain, R. Legras, Track-etch templates designed for micro- and nanofabrication, *Nucl. Inst. Methods Phys. Res. B Beam Interactions Mater. Atoms* 208 (2003) 115–122, [https://doi.org/10.1016/S0168-583X\(03\)00637-2](https://doi.org/10.1016/S0168-583X(03)00637-2).
- [18] T. da Câmara Santa Clara Gomes, J. de la Torre Medina, Y.G. Velázquez-Galván, J.M. Martínez-Huerta, A. Encinas, L. Piraux, Interplay between the magnetic and

- magneto-transport properties of 3D interconnected nanowire networks., *J. Appl. Phys.* 120 (4) (2016) 043904, <https://doi.org/10.1063/1.4959249>.
- [19] T. da Câmara Santa Clara Gomes, J. De La Torre Medina, M. Lemaitre, L. Piraux, Magnetic and magnetoresistive properties of 3D interconnected NiCo nanowire networks, *Nanoscale Res. Lett.* 11 (1) (2016) 466, <https://doi.org/10.1186/s11671-016-1679-z>.
- [20] G. Hrkac, J. Dean, D.A. Allwood, Nanowire spintronics for storage class memories and logic, *Philos. Trans. R. Soc. A Math. Phys. Eng. Sci.* 369 (1948) (2011) 3214–3228, <https://doi.org/10.1098/rsta.2011.0138>.
- [21] J. Escrig, M. Daub, P. Landeros, K. Nielsch, D. Altbir, Angular dependence of coercivity in magnetic nanotubes, *Nanotechnology* 18 (44) (2007) 445706. <http://stacks.iop.org/0957-4484/18/i=44/a=445706>.
- [22] S. Allende, J. Escrig, D. Altbir, E. Salcedo, M. Bahiana, Angular dependence of the transverse and vortex modes in magnetic nanotubes, *Eur. Phys. J. B* 66 (1) (2008) 37–40, <https://doi.org/10.1140/epjbe2008-00385-4>.
- [23] O. Albrecht, R. Zierold, S. Allende, J. Escrig, C. Patzig, B. Rauschenbach, K. Nielsch, D. Görlitz, Experimental evidence for an angular dependent transition of magnetization reversal modes in magnetic nanotubes, *J. Appl. Phys.* 109 (9) (2011) 093910, <https://doi.org/10.1063/1.3583666>.
- [24] M.P. Proenca, C.T. Sousa, J. Escrig, J. Ventura, M. Vazquez, J.P. Araujo, Magnetic interactions and reversal mechanisms in Co nanowire and nanotube arrays, *J. Appl. Phys.* 113 (9) (2013) 093907, <https://doi.org/10.1063/1.4794335>.
- [25] Y. Velázquez-Galván, J.M. Martínez-Huerta, J. de la Torre Medina, Y. Danlée, L. Piraux, A. Encinas, Dipolar interaction in arrays of magnetic nanotubes. *J. Phys. Condensed Matter* 26 (2) (2014) 026001. <http://stacks.iop.org/0953-8984/26/i=2/a=026001>.
- [26] J. de la Torre Medina, T. da Câmara Santa Clara Gomes, Y.G. Velázquez Galván, L. Piraux, Large-scale 3-D interconnected Ni nanotube networks with controlled structural and magnetic properties., *Sci. Rep.* 8 (1) (2018) 14555, <https://doi.org/10.1038/s41598-018-32437-8>.
- [27] J. He, T.M. Tritt, Advances in thermoelectric materials research: looking back and moving forward, *Science* 357 (6358) (2017), <https://doi.org/10.1126/science.aak9997>.
- [28] G.E.W. Bauer, E. Saitoh, B.J. van Wees, Spin caloritronics, *Nat. Mater.* 11 (2012) 391 EP, <https://doi.org/10.1038/nmat3301>.
- [29] S.R. Boona, R.C. Myers, J.P. Heremans, Spin caloritronics, *Energy Environ. Sci.* 7 (2014) 885–910, <https://doi.org/10.1039/C3EE43299H>.
- [30] K. Uchida, J. Xiao, H. Adachi, J. Ohe, S. Takahashi, J. Ieda, T. Ota, Y. Kajiwara, H. Umezawa, H. Kawai, G.E.W. Bauer, S. Maekawa, E. Saitoh, Spin Seebeck insulator, *Nat. Mater.* 9 (2010) 894 EP, <https://doi.org/10.1038/nmat2856>.
- [31] C.M. Jaworski, J. Yang, S. Mack, D.D. Awschalom, J.P. Heremans, R.C. Myers, Observation of the spin-Seebeck effect in a ferromagnetic semiconductor, *Nat. Mater.* 9 (2010) 898 EP, <https://doi.org/10.1038/nmat2860>.
- [32] A. Slachter, F.L. Bakker, J.-P. Adam, B.J. van Wees, Thermally driven spin injection from a ferromagnet into a non-magnetic metal, *Nat. Phys.* 6 (2010) 879 EP, <https://doi.org/10.1038/nphys1767>.
- [33] M. Hatami, G.E.W. Bauer, Q. Zhang, P.J. Kelly, Thermal spin-transfer torque in magnetoelectronic devices, *Phys. Rev. Lett.* 99 (2007) 066603, <https://doi.org/10.1103/PhysRevLett.99.066603>.

- [34] A. Pushp, T. Phung, C. Rettner, B.P. Hughes, S.-H. Yang, S.S.P. Parkin, Giant thermal spin-torque-assisted magnetic tunnel junction switching, *Proc. Natl. Acad. Sci.* 112 (21) (2015) 6585–6590, <https://doi.org/10.1073/pnas.1507084112>.
- [35] T. da Câmara Santa Clara Gomes, F. Abreu Araujo, L. Piraux, Making flexible spin caloritronic devices with interconnected nanowire networks, *Sci. Adv.* 5 (3) (2019) eaav2782, <https://doi.org/10.1126/sciadv.aav2782>.
- [36] F. Abreu Araujo, T. da Câmara Santa Clara Gomes, L. Piraux, Magnetic control of flexible thermoelectric devices based on macroscopic 3D interconnected nanowire networks, *Adv. Electron. Mater.* 5 (2019)1800919.
- [37] Q. Wang, G. Wang, X. Han, X. Wang, J.G. Hou, Controllable template synthesis of Ni/Cu nanocable and Ni nanotube arrays: a one-step coelectrodeposition and electrochemical etching method, *J. Phys. Chem. B* 109 (49) (2005) 23326–23329, <https://doi.org/10.1021/jp0530202>.
- [38] Z. Liu, G. Xia, F. Zhu, S. Kim, N. Markovic, C.-L. Chien, P.C. Searson, Exploiting finite size effects in a novel core/shell microstructure, *J. Appl. Phys.* 103 (6) (2008) 064313, <https://doi.org/10.1063/1.2844286>.
- [39] V.-A. Antohe, E. Nysten, J.M. Martínez-Huerta, P.M. Pereira de Sá, L. Piraux, Annealing effects on the magnetic properties of highly-packed vertically-aligned nickel nanotubes, *RSC Adv.* 7 (2017) 18609–18616, <https://doi.org/10.1039/C7RA01276D>.
- [40] L. Piraux, J.M. George, J.F. Despres, C. Leroy, E. Ferain, R. Legras, K. Ounadjela, A. Fert, Giant magnetoresistance in magnetic multilayered nanowires, *Appl. Phys. Lett.* 65 (19) (1994) 2484–2486, <https://doi.org/10.1063/1.112672>.
- [41] A. Fert, L. Piraux, Magnetic nanowires, *J. Magn. Magn. Mater.* 200 (1) (1999) 338–358, [https://doi.org/10.1016/S0304-8853\(99\)00375-3](https://doi.org/10.1016/S0304-8853(99)00375-3).
- [42] J.-E. Wegrowe, D. Kelly, A. Franck, S.E. Gilbert, J.-P. Ansermet, Magnetoresistance of ferromagnetic nanowires, *Phys. Rev. Lett.* 82 (1999) 3681–3684, <https://doi.org/10.1103/PhysRevLett.82.3681>.
- [43] S. Pignard, G. Goglio, A. Radulescu, L. Piraux, S. Dubois, A. Declémy, J.L. Duvail, Study of the magnetization reversal in individual nickel nanowires, *J. Appl. Phys.* 87 (2) (2000) 824–829, <https://doi.org/10.1063/1.371947>.
- [44] T. Ohgai, L. Gravier, X. Hoffer, M. Lindeberg, K. Hjort, R. Spohr, J.-P. Ansermet, Template synthesis and magnetoresistance property of Ni and Co single nanowires electrodeposited into nanopores with a wide range of aspect ratios, *J. Phys. D Appl. Phys.* 36 (24) (2003) 3109.
- [45] T. da Câmara Santa Clara Gomes, J. De La Torre Medina, Y.G. Velázquez-Galván, J. M. Martínez-Huerta, A. Encinas, L. Piraux, 3-D interconnected magnetic nanofiber networks with multifunctional properties, *IEEE Trans. Magn.* 53 (11) (2017) 1–6, <https://doi.org/10.1109/TMAG.2017.2719658>.
- [46] T. McGuire, R. Potter, Anisotropic magnetoresistance in ferromagnetic 3D alloys, *IEEE Trans. Magn.* 11 (4) (1975) 1018–1038, <https://doi.org/10.1109/TMAG.1975.1058782>.
- [47] M. Darques, A. Encinas, L. Vila, L. Piraux, Controlled changes in the microstructure and magnetic anisotropy in arrays of electrodeposited Co nanowires induced by the solution pH, *J. Phys. D Appl. Phys.* 37 (10) (2004) 1411.
- [48] J. de la Torre Medina, G. Hamoir, Y. Velázquez-Galván, S. Pouget, H. Okuno, L. Vila, A. Encinas, L. Piraux, Large magnetic anisotropy enhancement in size controlled Ni nanowires electrodeposited into nanoporous alumina templates., *Nanotechnology* 27 (14) (2016) 145702.

- [49] B.G. Tóth, L. Péter, Á. Révész, J. Pádár, I. Bakonyi, Temperature dependence of the electrical resistivity and the anisotropic magnetoresistance (AMR) of electrodeposited Ni-Co alloys, *Eur. Phys. J. B* 75 (2) (2010) 167–177, <https://doi.org/10.1140/epjb/e2010-00132-4>.
- [50] N.V. Myung, K. Nobe, Electrodeposited iron group thin-film alloys: structure-property relationships, *J. Electrochem. Soc.* 148 (3) (2001) C136–C144, <https://doi.org/10.1149/1.1345875>.
- [51] Z. Liu, D. Elbert, C.-L. Chien, P.C. Searson, FIB/TEM characterization of the composition and structure of core/shell Cu-Ni nanowires, *Nano Lett.* 8 (8) (2008) 2166–2170.
- [52] J.M. Martínez-Huerta, J. de la Torre Medina, L. Piraux, A. Encinas, Self consistent measurement and removal of the dipolar interaction field in magnetic particle assemblies and the determination of their intrinsic switching field distribution., *J. Appl. Phys.* 111 (8) (2012) 083914.
- [53] D. Ruffer, R. Huber, P. Berberich, S. Albert, E. Russo-Averchi, M. Heiss, J. Arbiol, A. Fontcuberta i Morral, D. Grundler, Magnetic states of an individual Ni nanotube probed by anisotropic magnetoresistance, *Nanoscale* 4 (16) (2012) 4989–4995.
- [54] F.J. Blatt, P.A. Schroeder, C.L. Foiles, D. Greig, *Thermoelectric Power of Metals*, Springer, Boston, MA, 1976.
- [55] S.J. Watzman, R.A. Duine, Y. Tserkovnyak, S.R. Boona, H. Jin, A. Prakash, Y. Zheng, J. P. Heremans, Magnon-drag thermopower and Nernst coefficient in Fe, Co, and Ni, *Phys. Rev. B* 94 (2016) 144407, <https://doi.org/10.1103/PhysRevB.94.144407>.
- [56] K. Vandaele, S.J. Watzman, B. Flebus, A. Prakash, Y. Zheng, S.R. Boona, J.P. Heremans, Thermal spin transport and energy conversion, *Mater. Today Phys.* 1 (2017) 39–49, <https://doi.org/10.1016/j.mtphys.2017.05.003>.
- [57] D.K.C. MacDonald, *Thermoelectricity: An Introduction to the Principles*, Wiley, New York, NY, 1962.
- [58] J. de la Torre Medina, M. Darques, A. Encinas, L. Piraux, Dipolar interactions in multilayered Co<sub>0.96</sub>Cu<sub>0.04</sub>/Cu nanowire arrays., *Phys. Stat. Sol. (a)* 205 (8) (2008) 1813–1816, <https://doi.org/10.1002/pssa.200723622>.
- [59] O. Yamashita, S. Tomiyoshi, K. Makita, Bismuth telluride compounds with high thermoelectric figures of merit, *J. Appl. Phys.* 93 (1) (2002) 368–374, <https://doi.org/10.1063/1.1525400>.
- [60] O. Bubnova, Z.U. Khan, A. Malti, S. Braun, M. Fahlman, M. Berggren, X. Crispin, Optimization of the thermoelectric figure of merit in the conducting polymer poly(3,4-ethylenedioxythiophene), *Nat. Mater.* 10 (2011) 429 EP, <https://doi.org/10.1038/nmat3012>.
- [61] M.N. Ou, T.J. Yang, S.R. Harutyunyan, Y.Y. Chen, C.D. Chen, S.J. Lai, Electrical and thermal transport in single nickel nanowire, *Appl. Phys. Lett.* 92 (6) (2008) 063101, <https://doi.org/10.1063/1.2839572>.
- [62] A.B. Cahaya, O.A. Tretiakov, G.E.W. Bauer, Spin Seebeck power generators, *Appl. Phys. Lett.* 104 (4) (2014) 042402, <https://doi.org/10.1063/1.4863084>.
- [63] S.F. Lee, W.P. Pratt, R. Loloee, P.A. Schroeder, J. Bass, “Field-dependent interface resistance” of Ag/Co multilayers, *Phys. Rev. B* 46 (1992) 548–551, <https://doi.org/10.1103/PhysRevB.46.548>.
- [64] J. Bass, CPP magnetoresistance of magnetic multilayers: a critical review, *J. Magn. Magn. Mater.* 408 (2016) 244–320, <https://doi.org/10.1016/j.jmmm.2015.12.011>.
- [65] T. Farrell, D. Greig, The thermoelectric power of nickel and its alloys, *J. Phys. C Solid State Phys.* 3 (1) (1970) 138.

- 
- [66] M.C. Cadeville, J. Roussel, Thermoelectric power and electronic structure of dilute alloys of nickel and cobalt with d transition elements, *J. Phys. F Metal Phys.* 1 (5) (1971) 686.
- [67] J. Shi, S.S.P. Parkin, L. Xing, M.B. Salamon, Giant magnetoresistance and magnetothermopower in Co/Cu multilayers, *J. Magn. Magn. Mater.* 125 (3) (1993) L251–L256, [https://doi.org/10.1016/0304-8853\(93\)90094-I](https://doi.org/10.1016/0304-8853(93)90094-I).
- [68] F.K. Dejene, J. Flipse, B.J. van Wees, Spin-dependent Seebeck coefficients of  $\text{Ni}_{80}\text{Fe}_{20}$  and Co in nanopillar spin valves, *Phys. Rev. B* 86 (2012) 024436, <https://doi.org/10.1103/PhysRevB.86.024436>.